Geophysical Journal International

*Geophys. J. Int.* (2010) **182,** 531–550 doi: 10.1111/j.1365-246X.2010.04641.x

# Uplift at lithospheric swells—I: seismic and gravity constraints on the crust and uppermost mantle structure of the Cape Verde mid-plate swell

D. J. Wilson,[1] C. Peirce,[1] A. B. Watts,[2] I. Grevemeyer[3] and A. Krabbenhoeft[3]

[1]*Department of Earth Sciences, Durham University, South Road, Durham* DH1 3LE, *UK. Email: christine.peirce@durham.ac.uk*
[2]*Department of Earth Sciences, University of Oxford, Oxford,* OX1 3PR, *UK*
[3]*Leibniz-Institute of Marine Sciences, IFM-GEOMAR, East Shore Campus, Wischhofstr.* 1-3, D-24148 *Kiel, Germany*

Accepted 2010 April 26. Received 2010 April 19; in original form 2009 December 17



## SUMMARY

Wide-angle seismic data have been used to determine the velocity and density structure of the crust and uppermost mantle beneath the Cape Verdes mid-plate swell. Seismic modelling reveals a 'standard' oceanic crust, ∼8 km in thickness, with no direct evidence for low-density bodies at the base of the crust. Gravity anomaly modelling within the constraints and resolution provided by the seismic model, does not preclude, however, a layer of crustal underplate up to 3 km thick beneath the swell crest. The modelling shows that while the seismically constrained crustal structure accounts for the short-wavelength free-air gravity anomaly, it fails to fully explain the long-wavelength anomaly. The main discrepancy is over the swell crest where the gravity anomaly, after correcting for crustal structure, is higher by about 30 mGal than it is over its flanks. The higher gravity can be explained if the top 100 km of the mantle beneath the swell crest is less dense than its surroundings by 30 kg $m^{-3}$. The lack of evidence for low densities and velocities in the uppermost mantle, and high densities and velocities in the lower crust, suggests that neither a depleted swell root or crustal underplate are the origin of the observed shallower-than-predicted bathymetry and that, instead, the swell is most likely supported by dynamic uplift associated with an anomalously low density asthenospheric mantle.

**Key words:** Controlled source seismology; Intraplate processes; Oceanic hotspots and intraplate volcanism; Lithospheric flexure; Crustal structure.

## 1 INTRODUCTION

The oceanic lithosphere is created at mid-ocean ridges and increases its long-term strength as it cools and subsides with age (e.g. Watts & Zhong 2000; Watts & Burov 2003). Acting as the outer thermal mechanical boundary layer of the solid Earth, the oceanic lithosphere also transfers excess heat, above background radiogenic production, from the underlying asthenosphere to the hydrosphere. A characteristic pattern of cooling and subsidence, increasing from the ridge axis to the continental margin, has been developed based on an exponential decrease in heat flow and increase in bathymetry with age (Davis & Lister 1974; Sclater *et al.* 1980). Since this correlation was first recognized, many anomalous bathymetric highs have been identified throughout the ocean basins (e.g. Marty & Cazenave 1989). These regions, or swells as they are commonly called, range in size up to 2000 km in diameter, with topography up to 2.5 km shallower than that expected based on plate age alone (Crough 1983; Stein & Stein 1992).

Oceanic mid-plate swells are also associated with long-wavelength gravity and geoid anomaly highs and excess heat flow (e.g. Crough & Jurdy 1980; Pollack *et al.* 1993), implying that the lithosphere is thermally reheated and/or mechanically weakened in some way, and are often accompanied by extensive and locally concentrated intraplate volcanism. These intraplate sites of persistent, long-term volcanic activity have been termed 'hotspots' (Wilson 1963) on account of the vast volumes of melt produced from the mantle without the aid of external tectonic forces, and are often associated with a similar scale of volcanism to that observed at plate boundaries. Examples of this hotspot-related volcanism are seamounts and oceanic islands superimposed upon the associated regional topographic swells and include Hawaii (Watts *et al.* 1985), the Canary Islands (Watts *et al.* 1997), the Marquesas Islands (Caress *et al.* 1995), the Cape Verde Islands (Pim *et al*. 2008; Grevemeyer *et al*. 2010) and the Society Islands (Grevemeyer *et al.* 2001b).

Geochemical $^{40}Ar/^{39}Ar$ dating of ocean island basalts also reveals that hotspots may be intermittently active for >100 Ma, often with more than 5 Ma between major eruptive phases, and some can be traced back to large igneous provinces using the age-progression of island chains and records of palaeoplate motions (Duncan &

Richards 1991). The magnitude and longevity of hotspots therefore implies that they are the surface expressions of a significant melting process that may also act to dissipate excess heat energy from the deep interior.

One hypothesis for the formation of hotspots is that hot (low density) material rises from deep in the mantle, and interacts with the base of the crust (Sleep 1992; Ribe & Christensen 1994; Cserepes *et al.* 2000). Another is that weak zones in the lithosphere or crust, perhaps unusually thin or fractured, lead to preferential pathways for the injection and eruption of melt from the mantle (Turcotte & Oxburgh 1973; McNutt *et al.* 1997). Formation of hotspot-related volcanic edifices occurs either contemporaneously with crustal accretion at a mid-ocean ridge axis, for example at zero-plate age, or any time subsequently in a mid-plate setting as the underlying plate mechanically ages. No matter when they are constructed, these volcanic edifices represent a downward-acting force and undergo subsidence in order to maintain isostatic equilibrium as the plate on which they sit flexes under the load.

For a defined load of specific volume and density, the amplitude and wavelength of the associated subsidence is dependent upon the mechanical structure of the lithosphere. The elastic thickness, $T_e$, is a proxy for the long-term ($>10^5$ a) strength of the lithosphere. Lithosphere with a low $T_e$ is weak and subsidence is confined to a concentrated area of deformation directly beneath the load, whereas lithosphere with a high $T_e$ is strong and the total subsidence is accommodated within a larger region of lower amplitude flexure. Consequently, the ability to image marker interfaces within the crust that represent the amplitude and wavelength of the load-associated subsidence, enables the long-term thermal and mechanical properties of the lithosphere to be constrained. The flexural markers, in turn, can be used to determine the extent of modification to the thermomechanical structure of the lithosphere as a result of heating by sub-, intra- and extraplate magmatic processes (e.g. Ali *et al.* 2003).

Analysis of multichannel seismic (MCS) reflection data provides a means of mapping the geometry of such horizons within the sediment column, such as unconformities, which reflect major phases of subsidence or uplift. Wide-angle (WA) refraction data, on the other hand, not only provide velocities for depth conversion and subsequent top-of-plate load volume and mass calculation, but can also be interpreted to infer the extent of, if any, crustal thickening by underplating or intracrustal density change as a result of magmatic intrusion.

Such observed horizons can be compared to those predicted from elastic plate flexure models using an oceanic lithosphere with a $T_e$ based on its expected age derived from magnetic anomalies. Any mismatch between the calculated and observed flexural surfaces implies an anomalous lithosphere. If, for example, the observed flexure is less pronounced than that predicted, then this implies that subsurface forces are acting to support the surface load (e.g. Watts & ten Brink 1989). If more pronounced, it implies that the lithosphere has been mechanically rejuvenated.

Comparison of bathymetric and geoid anomalies to the expected values for standard oceanic lithosphere together with evidence from flexural horizon modelling, suggests that there is some form of regional load support acting at mid-plate swells. Several mechanisms have been proposed to explain how large-scale topographic swells are sustained over geological timescales (Fig. 1, based on Crough 1983):

1. Shallow support within the crust (Fig. 1a)—e.g. Morgan *et al.* (1995). The eruption of volcanic islands on top of the oceanic lithosphere is often accompanied by underplating, the intrusive accumulation of neutrally buoyant magma at the base of the crust (e.g. Charvis *et al.* 1999; Grevemeyer *et al.* 2001b). A thickened oceanic basement provides additional buoyancy, due to its lower density relative to the surrounding mantle, analogous to the deep crustal roots that support continental mountain belts.

2. Support within the upper mantle (Fig. 1b)—e.g. Detrick & Crough (1978) and Robinson (1988). A region of low density in the lithospheric mantle, either due to an elevated temperature or compositional variation, may provide sufficient upwards force to elevate the lithosphere. Morgan *et al.* (1995) observed a strong correlation between the volume of oceanic volcanism and the size of the associated bathymetric swell along the Hawaiian chain, and show that the density reduction in the lithospheric mantle and the upper asthenosphere due to thermal reheating and basaltic melt extraction contributes significantly to swell topography.

3. Dynamic mantle upwelling (Fig. 1c)—e.g. Sleep (1995). Material actively rising through the asthenosphere acts as a negative load on the base of the lithosphere that causes flexure of the entire plate. Monnereau *et al.* (1993) used numerical models to simulate dynamic uplift resulting from the ascent of low density material through a convective mantle to the base of a rigid lithosphere. Uplift was observed to occur in two stages: pure dynamical support during initial ascent, and a larger stage of uplift following ductile

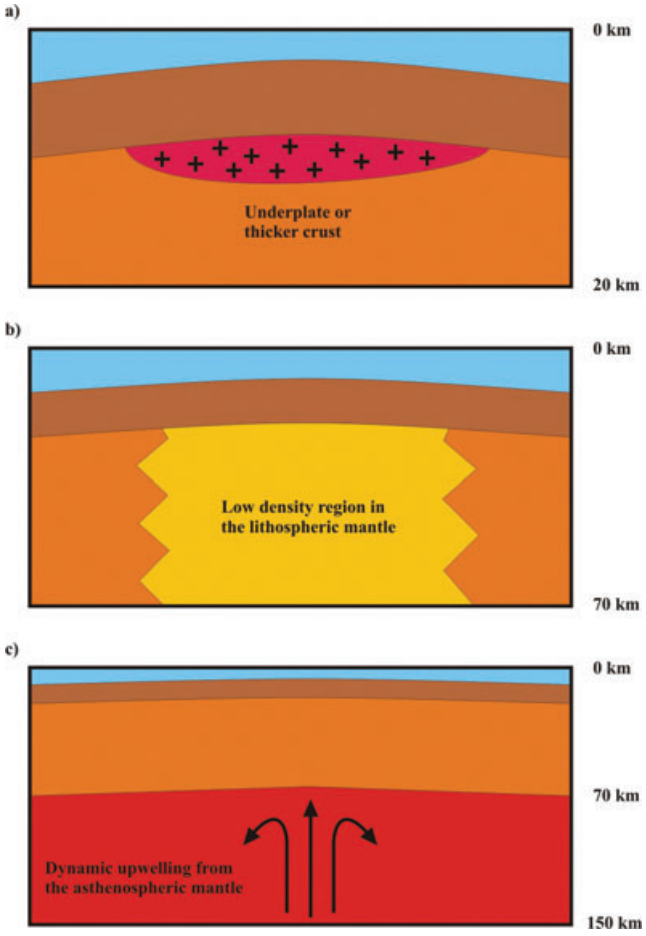


**Figure 1.** Mechanisms proposed to explain how large-scale topographic swells are sustained over geological timescales (after Crough 1983). (a) Shallow support in the crust. (b) Support in the lithospheric mantle. (c) Upwelling in the asthenospheric mantle.

thinning of the lithosphere as the upwelled material impinges on the convective boundary layer.

In this paper, we present the results of analysis and forward modelling of a WA seismic refraction dataset acquired along an ∼475 km profile through the Cape Verde archipelago; a chain of volcanic islands superimposed on the crest of the Cape Verde mid-plate swell. Traveltime data are iteratively modelled using a ray tracing approach to produce a 2-D velocity–depth model of the crust and uppermost mantle. The resulting velocity–density–depth model is then tested against the coincident MCS-derived flexural horizons and shipboard and satellite free-air gravity anomaly (FAA) data for uniqueness and consistency.

Ultimately, the Cape Verdes study aims to evaluate the three proposed swell support mechanisms using various forward modelling methods applied to a range of observed geophysical data, as well as investigate the origin of swells. Anomalously thick crust would suggest that a swell is an old feature that originated during enhanced magmatic crustal accretion at a mid-ocean ridge, perhaps under the influence of enhanced mantle upwelling. Normal thickness crust would imply that a swell is a post-accretion feature, possibly related to vertical motion in the underlying mantle. Here, we take the first steps to resolving the origin of the uplift observed at the Cape Verde mid-plate swell by first resolving the lateral and vertical variation in layering structure and density within the 'background' crust which, in turn, will act as well-constrained input into plate flexure and thermal structure modelling of the whole plate, by allowing the superimposed shorter wavelength anomalies to be accounted for and removed. This 'whole plate' modelling, and a consideration of the geoid anomaly, will be presented in a subsequent paper.

## 2 TECTONIC SETTING

The Cape Verde Swell is the largest observed mid-plate swell on Earth; the approximately circular bathymetry anomaly alone encompasses a region 1800 km in diameter with a crest 2.2 km shallower than the surrounding abyssal plain, while the corresponding geoid anomaly reaches a maximum of +8 m (Monnereau & Cazenave 1990). Heat flow measurements show an increase from 43.5 mW $m^{-2}$ away from the influence of the swell to 60.5 mW $m^{-2}$ near the swell crest (Courtney & White 1986; Fig. 2), with the maximum heat flow anomaly 16 mW $m^{-2}$ higher, using the plate model of Parsons & Sclater (1977), than predicted for the (regional average) 130 Ma oceanic lithosphere on which the swell is imposed. The slow-to-stationary absolute motion of the African Plate in the Cape Verde region, $<$10 mm $yr^{-1}$ (Morgan 1983; Pollitz 1991), also results in a concentration of the associated uplift and volcanism into an approximately circular area and, consequently, makes this the ideal site to test the various proposed models for mid-plate swell support.

The Cape Verde archipelago is located ∼600 km off the coast of Senegal, West Africa, and is centred to the southwest of the crest of the associated swell. The cluster of nine main islands can be subdivided into a crescent of six islands to the southeast and a chain of three aligned towards the northwest (Fig. 2). Most of the island-building magmatism is thought to have occurred within the past 15 Ma (Stillman *et al.* 1982; Mitchell *et al.* 1983; Holm *et al.* 2008) and only Fogo has experienced historically recent volcanic activity. Magnetic anomalies M0–M21 can be identified in this region (Fig. 2), suggesting that the oceanic crust on which the islands were emplaced was accreted during the separation of the African continent from the Americas in the early Cretaceous (Albian to Berriasian, ∼110–150 Ma).

## 3 EXISTING DATA AND MODELS

The earliest seismic experiment in the Cape Verde region was by Dash *et al.* (1976) who undertook a refraction survey using land-based recording instruments deployed on the islands of Sal, Santiago and São Vicente. The data were analysed using a 1-D slope intercept method to determine the crustal structure along three split-spread profiles between the islands (Fig. 2). The resulting 1-D velocity–depth profiles indicate a velocity structure similar to that expected for standard oceanic crust (White *et al.* 1992), except for a consistently deeper Moho (16.2–16.7 km depth). However, these results are based on the assumptions of planar intracrustal layering and homogeneity within layers in the subsurface, and may reflect a bias towards local crustal thickening concentrated beneath the islands given the recording instrument locations.

Using MCS reflection and gravity data acquired during the 'RRS Charles Darwin' geophysical survey in 1985 (Fig. 2), Ali *et al.* (2003) mapped flexural horizons in the moat sediments of the islands and investigated the shallow crustal structure down to the igneous basement. By modelling the geometry of these markers, the degree of flexure could be quantified and compared to that obtained from numerical models of viscoelastic plates subjected to loads of comparable dimensions to the islands, to determine the $T_e$ of the underlying lithosphere. Their calculated $T_e$ of 29 km agrees with that predicted from the magnetic anomaly derived plate age predicted value, signifying that the lithosphere has not been significantly, if at all, thermally rejuvenated as part of load emplacement.

However, the interpretation (and subsequent modelling) of flexural markers picked in reflection data depends upon the accuracy of the time-to-depth conversion, which in turn depends on accurate velocity information. Only a few sparse and poor quality sources of velocity data were available to Ali *et al.* (2003), including: stacking velocities; a sonobuoy at the edge of their study area; and 1-D estimates from Dash *et al.* (1976). All of these velocity sources have limitations in accuracy, depth sampled below the surface and areal extent, and are far from ideal, even taken collectively.

Analysis of receiver functions from a temporary network of seismic recording stations on the Cape Verde islands has provided several additional 1-D estimates of crustal thickness and velocity–depth structure of the lithospheric mantle (Lodge & Helffrich 2006). The results have also been interpreted to suggest crustal thickening beneath some of the islands, but are unable to differentiate between models for localized crustal thickening related to island building, and regional underplating related to the support of the entire swell.

## 4 SEISMIC EXPERIMENT

The *R/V Meteor* cruise M62/3 conducted a marine geophysical survey over the Cape Verde mid-plate swell. The main objective of this cruise was to investigate the crust and upper mantle structure of the swell by means of a WA, controlled-source seismic refraction experiment. The location of the main seismic profile (a solely WA profile) across the swell was chosen to coincide with a MCS reflection profile acquired during *RRS Charles Darwin* cruise 8/85 (Ali *et al.* 2003) which would be used to inform the initial velocity–depth model in terms of the sediment column structure and geometry, and the depth to basement (defined here as the top of oceanic crustal layer 2—the extrusive sequence).

Ocean-bottom seismographs and hydrophones (OBS and OBH, respectively; henceforth collectively referred to as OBS for

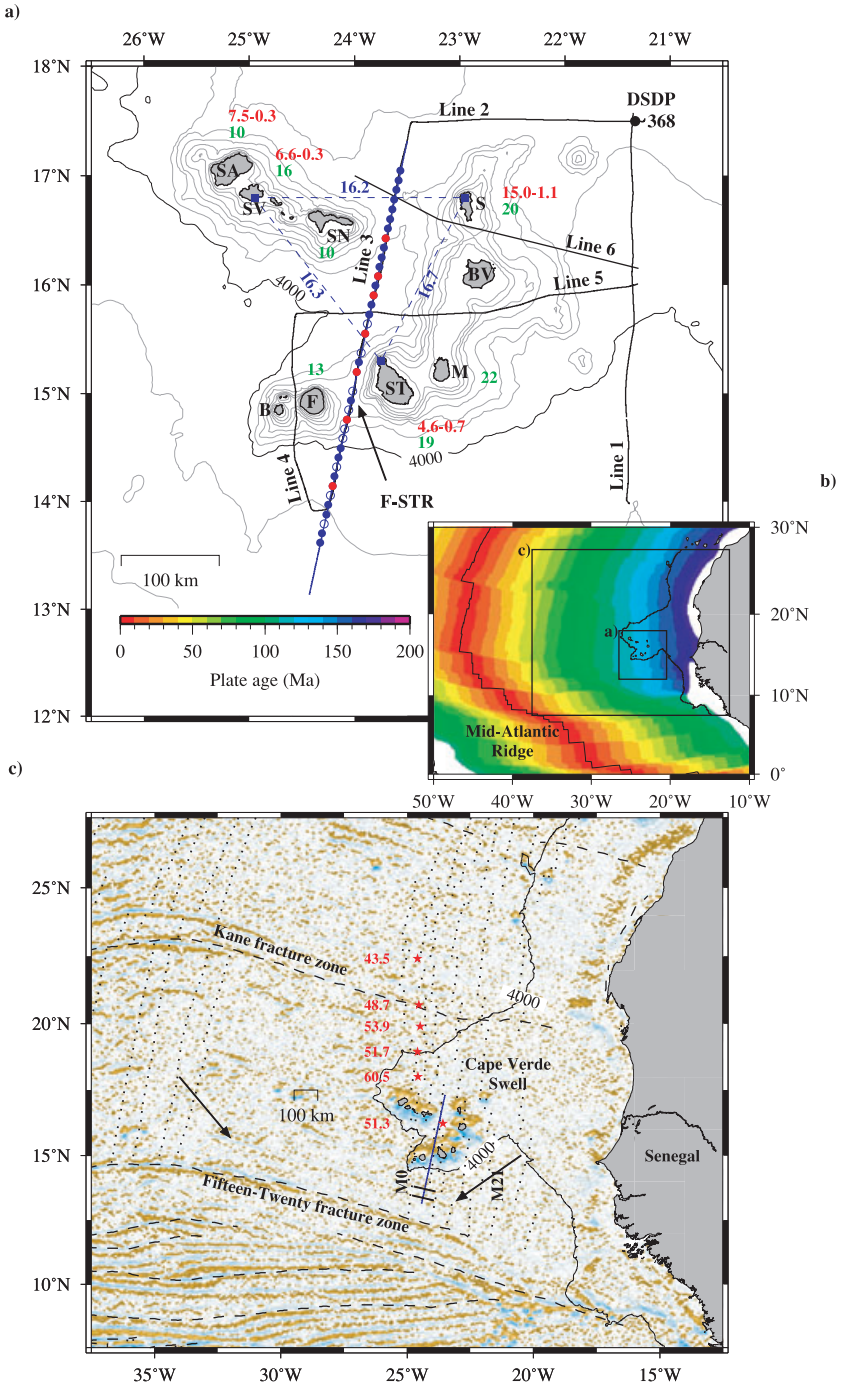


**Figure 2.** Geophysical surveys conducted at the Cape Verde archipelago and the tectonic setting of the Cape Verde Swell. The 4000 m bathymetric contour is used to outline the extent of the swell. (a) Location of MCS profiles from RRS Charles Darwin 1985 (black), see Ali *et al.* (2003), and the WA refraction profile from this study (blue). Filled/open blue circles mark OBS/OBH locations with red circles showing OBSs whose data is included in this paper. DSDP Site 368 is indicated with a black dot. Lodge & Helffrich's (2006) Moho depths, in km, beneath islands (green text) and Holm *et al.*'s (2006; 2008) volcanic evolution timescales, in Ma, (red text) are also shown together with Dash *et al*.'s (1976) 1-D seismic profiles and Moho depth determinations, in km (blue dashed lines and text). Islands: SA, Santo Antão; SV, São Vicente; SN, São Nicolau; S, Sal; BV, Boa Vista; M, Maio; ST, Santiago; F, Fogo; B, Brava. F-STR, Fogo-Santiago Ridge. Bathymetric contours (grey) with a 500 m contour interval. (b) Plate ages of Müller *et al*. (2008). Black boxes show the extent of the areas in (a) and (c). (c) The first derivative in latitude of the free-air gravity anomaly showing the locations of well-documented fracture-zones (dashed lines). A faint lineation can be observed trending perpendicular to the WA profile (as indicated by arrows) that intersects with the profile trend (blue line) at the southern end (as highlighted by parallel lines). Magnetic anomaly isochrons (dotted lines) show agreement with the plate ages in (b) and offsets correlate with fracture zone locations. Courtney & White's (1986) heat flow measurements, in mW $m^{-2}$ (red stars and text), show a positive heat flow anomaly over the Cape Verde Swell.

simplicity) were deployed at 10 km intervals along 390 km of the 475 km profile running north-south through the archipelago, intersecting the crest of the Cape Verde Swell at 16°00'N, 23°48'W (Fig. 2). OBS data were continuously recorded with a sampling rate of either 200 or 250 Hz, depending on instrument type (OBH or OBS, respectively). Swath bathymetry, gravity and magnetic data were also acquired contemporaneously along the profile. The seismic source consisted of eight airguns, configured as two subarrays towed at 8 m depth, and provided a total volume of ∼4000 in$^3$ (64 l). The source was triggered at 90 s intervals at a surveying speed of four knots, resulting in an average shot spacing of 180 m.

## 5 SEISMIC DATA

WA data were successfully recorded by 38 of the 40 instruments deployed, and example record sections showing features characteristic of all instruments are shown in Figs 3–6. Spectral analysis of these data shows that the seismic source had a frequency band of 5–30 Hz. On record sections with a high signal-to-noise ratio (SNR), arrivals can be identified to >60 km receiver offset (Fig. 3a). However, for instruments deployed on the crest of the Fogo-Santiago Ridge (F-STR) (Fig. 2), record sections have a low SNR (Fig. 3c) resulting in arrivals only being clearly observed at much shorter offsets.

Pim *et al.* (2008) present the results from a pilot study using a subset of the WA seismic and gravity data collected as part of *R/V Meteor* cruise M62/3. The aim of their study was to test the viability of the application of the data to 2-D seismic forward modelling and of the resultant velocity–depth model of a 2-D transect through the swell, as a crustal reference for 3-D flexure and gravity modelling of the entire swell. Pim *et al.*'s (2008) preliminary results show that the WA and gravity data can be best fit by a velocity–density–depth model which is not significantly different from standard oceanic crust and requires no underplate or regions of anomalous density in the lower crust or upper mantle, although this transect does not pass through any island and, thus, may also support Ali *et al.*'s (2003) conclusion that any underplate may be island load specific and not a major contributor to the swell.

Unlike Pim *et al.* (2008), who analysed the data from just nine instruments, in this paper we concentrated on the accurate identification of *P*-wave phases on both the hydrophone and vertical geophone record sections for all 38 instruments that recorded usable data. Primary refracted arrivals were grouped into four major phase types that could be correlated between adjacent instruments along the entire profile. The phase groups were labelled according to the expected subsurface structure, apparent *P*-wave velocities and receiver offset ranges (Fig. 3) as follows: a shallow subsurface arrival, $P_s$, which is often masked by other phases; two predominant crustal arrivals, $P_{g1}$ and $P_{g2}$; and upper mantle arrivals, $P_n$. In addition, the traveltimes of secondary arrivals reflected from the Moho, $P_mP$, were also picked.

Although the co-incident MCS data reveal a layer of sediment along all of the profile except at the F-STR, sediment arrivals are not distinguishable as clear first arrivals, being effectively obscured by the direct water wave and crustal arrivals, $P_{g1}$ and $P_{g2}$ (Fig. 3d). This absence of first-arriving sediment phases indicates that the sediment succession is relatively thin and/or has a low range of *P*-wave velocities. This conclusion is consistent with results of interpretation of the coincident and all regional MCS data (Fig. 7a; Ali *et al.* 2003) and cores from DSDP site 368 (Lancelot *et al.* 1978), which indicate sediment thicknesses of <2 km and bulk sediment *P*-wave velocities of <2.50 km s$^{-1}$, respectively.

### 5.1 Shallow subsurface arrival, $P_s$

The $P_s$ phase has an apparent velocity in the range 3.50–4.00 km s$^{-1}$, and the associated traveltime picks were assigned pick uncertainties in the range 20–30 ms. This phase is identified as a primary arrival at short receiver offsets (<10 km) exclusively on records from instruments deployed on the F-STR located between 220 and 310 km offset along the profile. The shot-receiver offset range over which this phase is observed increases heading towards the summit of the F-STR (250 km, profile offset), suggesting that the layer in which this arrival originates increases in thickness in this vicinity (Figs 3b and c). An absence of coherent reflectors is also noted in the MCS data in this region (Fig. 7). Instead, there is an intermittent high amplitude event beneath which reflections are chaotic and of high reflectivity, consistent with the reflection characteristics of igneous material erupted onto the seafloor or collapse debris from adjacent islands. These observations suggest that the F-STR is an intrasediment ridge comprising igneous material and only a thin veneer of sediment when compared to elsewhere along the profile.

### 5.2 Crustal arrivals, $P_{g1}$ and $P_{g2}$

Upper-mid crustal arrivals, $P_{g1}$, are identified as clear, high-amplitude arrivals with a high SNR along the entire profile at shot-receiver offsets of <10–15 km (Fig. 3e). These phases typically exhibit apparent velocities of 4.50–5.50 km s$^{-1}$, within the range expected for typical oceanic crustal layer 2 (White *et al.* 1992). The lateral variation in arrival time of the upper-mid crustal phase mirrors the topography of the basement surface.

The transition to the mid-lower crustal phase, $P_{g2}$, is mainly continuous (Fig. 3f), displaying a gradual increase in apparent velocity to 5.75 km s$^{-1}$ at the top of the layer, with the layer velocity increasing to 7.25 km s$^{-1}$ at the base, comparable to that of the gabbroic oceanic crustal layer 3 (White *et al.* 1992). Mid-lower crustal arrivals are consistently observed to shot-receiver offsets of 30–40 km, suggesting that there is no significant change in crustal thickness along the entire profile. $P_{g1}$ and $P_{g2}$ are assigned traveltime pick uncertainties increasing with offset from 20 to 40 ms.

### 5.3 Arrivals from the Moho and upper mantle, $P_mP$ and $P_n$

WA reflections from the Moho ($P_mP$ phase) are observed intermittently along the profile (Figs 3a and g). However, the presence of a Moho as a distinct interface is interpretable from the change in the apparent velocity of the first arrivals from 7.25 to 8.00 km s$^{-1}$ at ∼35 km shot-receiver offset, which is accompanied by a decrease in amplitude of the crustal arrivals (Fig. 3g). Unfortunately, the $P_n$ phase generally has a low SNR and is rarely observed at shot-receiver offsets >50 km. The assigned traveltime pick uncertainties are 50 ms for all $P_mP$ arrivals and range from 40 to 50 ms, assigned according to offset, for $P_n$ arrivals.

There is no evidence for the secondary WA reflections that have been observed at some intraplate settings (e.g. Watts *et al.* 1985; Caress *et al.* 1995; Grevemeyer *et al.* 2001a). Such mid-crustal reflections, together with unusually high lower crustal velocities (>7.3 km s$^{-1}$), have been interpreted as a relic Moho, which separates pre-hotspot crust from subcrustal underplate. The absence of these reflections in the data from the Cape Verdes implies that there has been no significant (i.e. thicker than the vertical resolution of the seismic data at that depth) volume of underplated material added to the base of the crust along the profile.

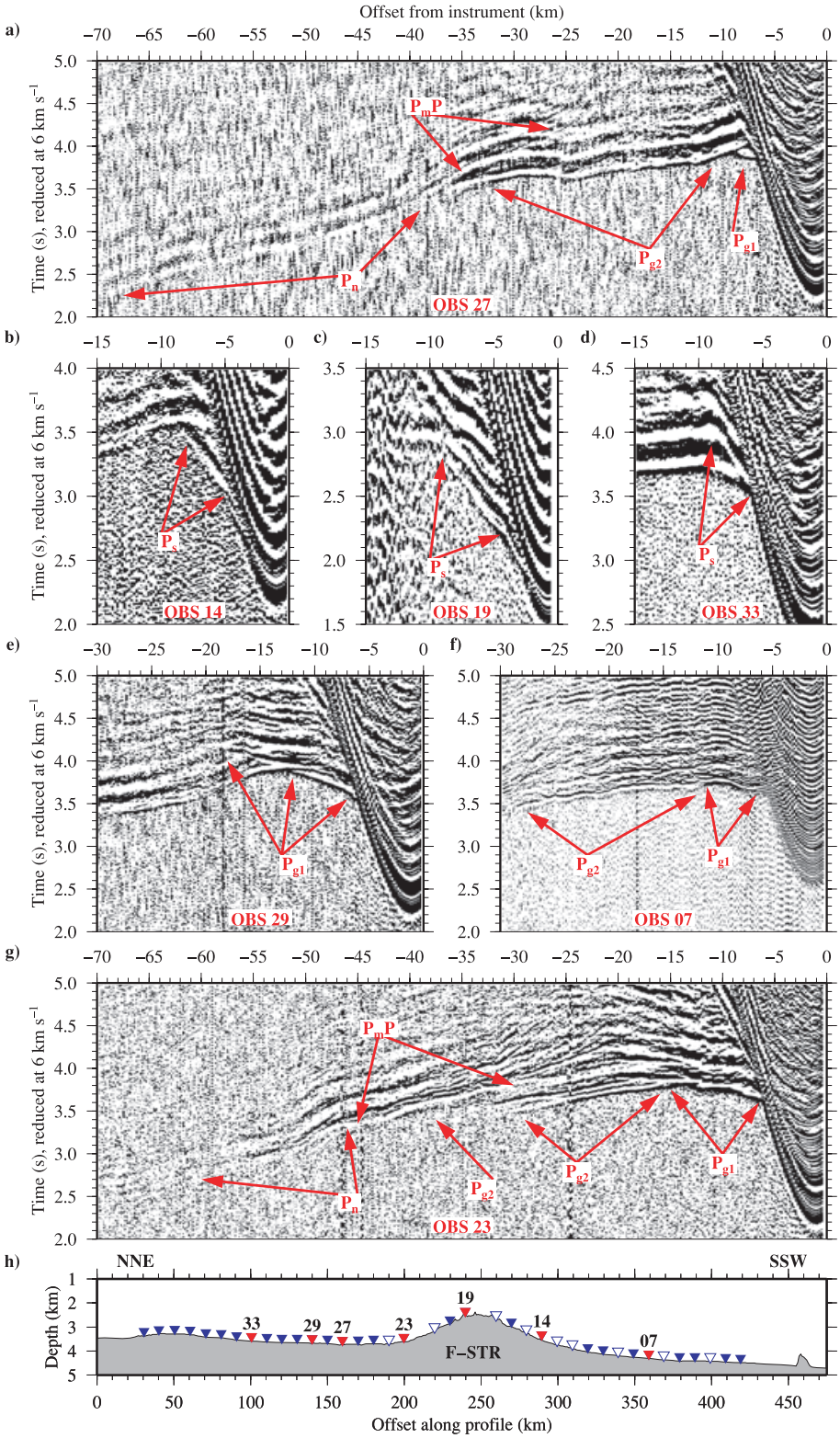


**Figure 3.** Examples of hydrophone data recorded on OBSs 14, 19, 23, 27, 29 and 33, and vertical geophone data recorded on OBS 07 (a)–(g). A bandpass filter of corner frequencies 0–5–35–40 Hz has been applied to the data. $P_s$, shallow subsurface arrivals; $P_{g1}$ and $P_{g2}$, crustal arrivals; $P_mP$, wide-angle reflections from the Moho; $P_n$, arrivals from the upper mantle. Record sections are plotted with a reduction velocity of 6 km s$^{-1}$. (h) Along-profile locations of instruments that successfully recorded data. Instruments from which the records in (a)–(g) are taken are highlighted in red. See Fig. 2 for transect location, definitions and abbreviations.

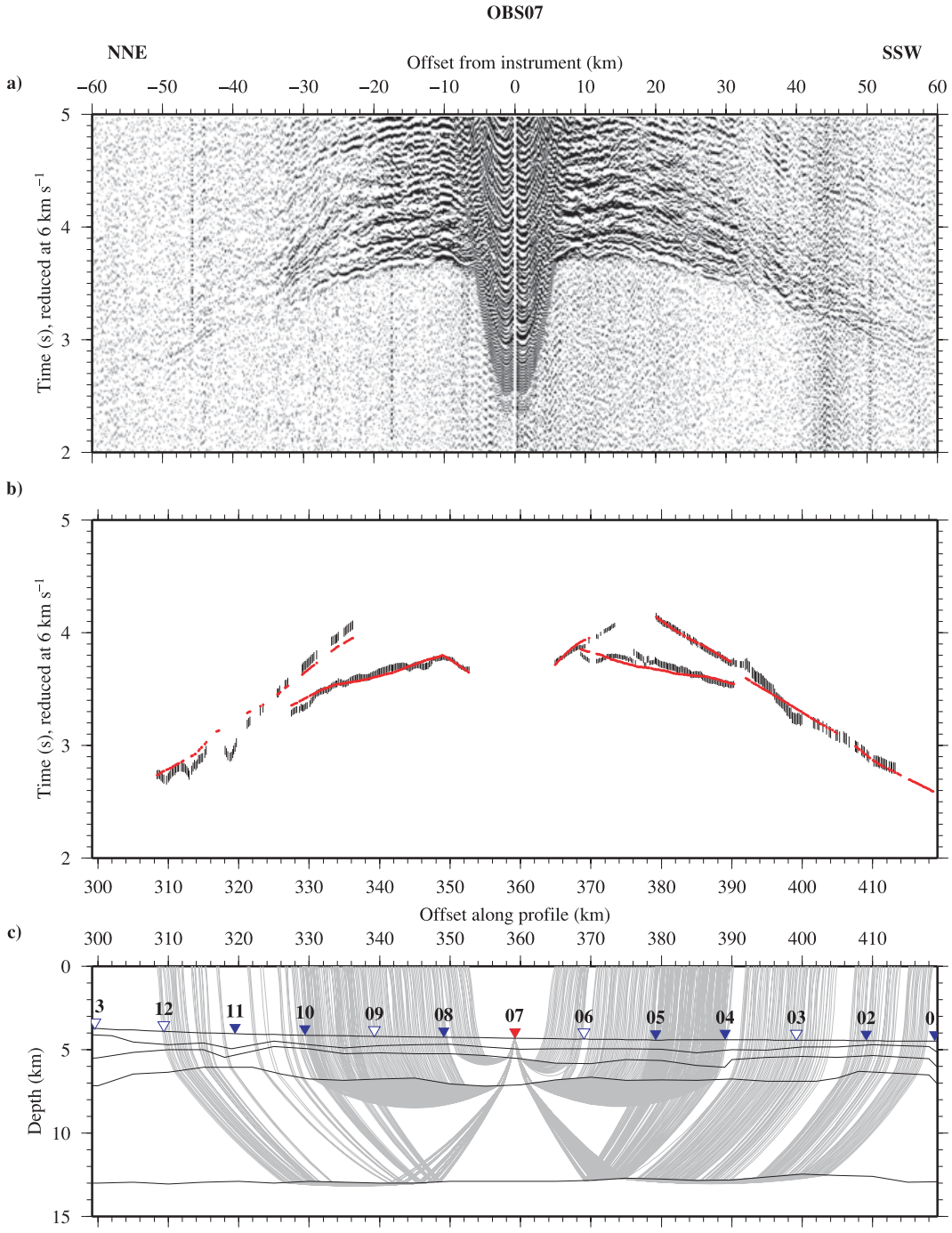


**Figure 4.** Ray-trace modelling of vertical geophone data recorded by OBS 07. (See Fig. 2 for instrument location). (a) Filtered record section plotted at true amplitude. (b) Observed traveltime picks (black vertical bars, representing the assigned picking error) and calculated traveltimes (red). (c) Ray diagram showing modelled arrivals. Record sections and traveltimes are plotted with a reduction velocity of 6 km s$^{-1}$.

### 5.4 MCS reflection data

Detailed analysis of the coincident MCS data provides an initial 2-D layer structure of the sediment stratigraphy along the profile. Ali *et al.* (2003) divide the sediment column into four layers based on the interpretation of key intrasediment horizons separating similar reflector packages (Fig. 7a), and using a detailed description of seismic facies for all profiles from *RRS Charles Darwin* cruise 8/85, of which Lines 2 and 5 intersect with the swell transect (Ali *et al.*'s 2003 Line 3; see Fig. 2 for profile location).

However, for the purposes of this study only the main units which demonstrate the load-related flexure are required, as these are necessary for the 'whole plate' modelling which will be presented in a subsequent paper, and so the sediment column was more simply divided into two layers, separated by an angular unconformity interpreted as representing the onset of subsidence due to surface loading, as follows.

*Layer 1*: Mesozoic sediments derived from the West African margin which formed following the rifting apart of North America and Africa and the formation of the North Atlantic ocean basin.

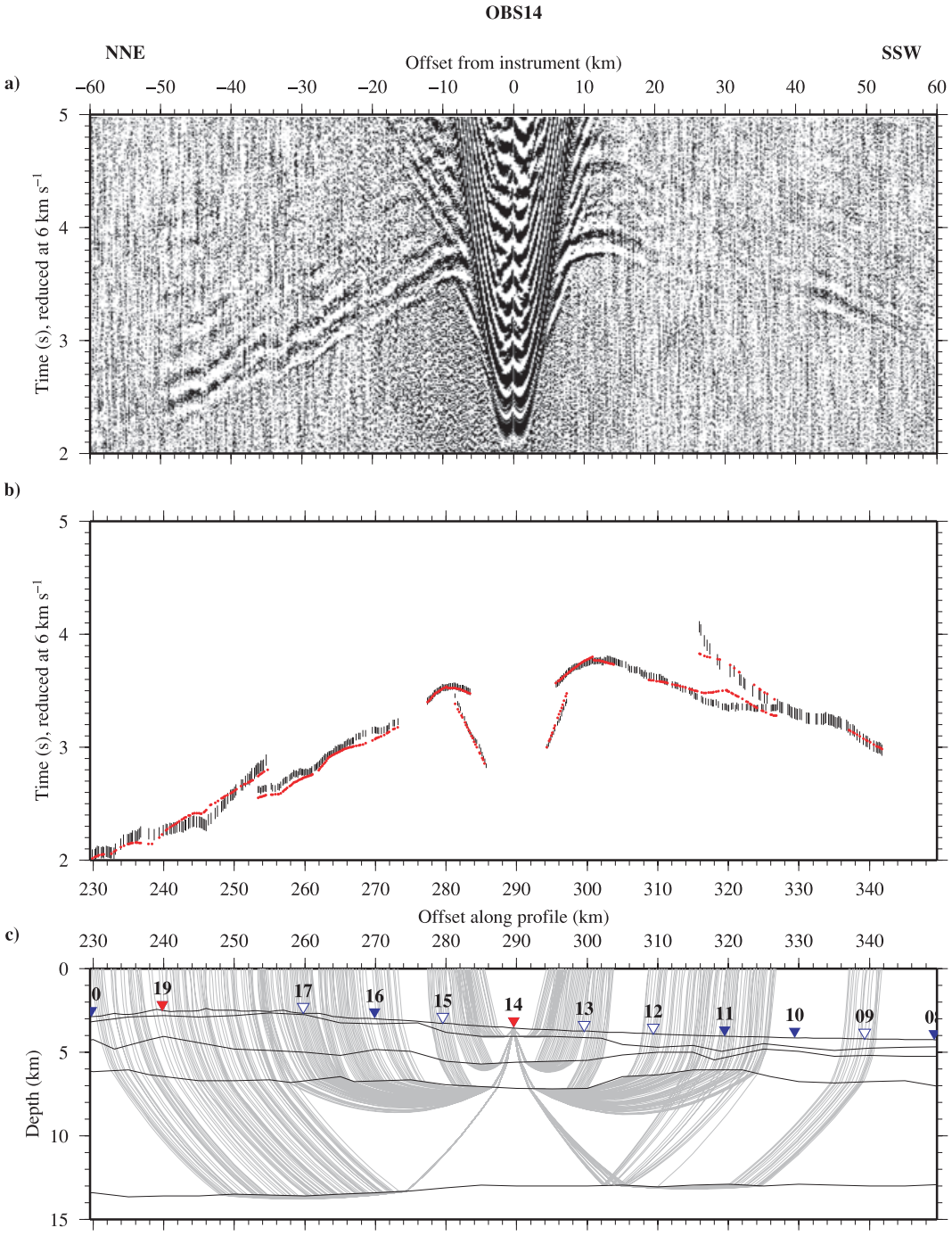


**Figure 5.** Ray-trace modelling of hydrophone data recorded by OBS 14. See Fig. 4 for details.

*Layer 2*: Neogene volcaniclastic sediments derived from the islands and pelagic sediments infilling the flexural moats formed by island-related plate loading.

The lack of primary sediment arrivals in the WA data requires interval velocities (to allow depth conversion of the unconformity reflection traveltime picks) to be sourced from a combination of standard sediment relationships (Hamilton 1978), Ali *et al.*'s (2003) stacking velocities, Dash *et al.*'s (1976) 1-D model and DSDP drilling logs (Lancelot *et al.* 1978) to facilitate the construction of the initial velocity–depth model. Although there are no directly observable arrivals from these layers, they will be included in the WA data modelling as described later except beneath the F-STR where the layer characteristics will be modified to match the observed $P_s$ phase, 'basement high', arrivals.

It is worth noting at this point that sediment layer velocities from the final WA model (see Section 7) will ultimately be used to convert the two-way traveltime picks of the MCS-derived flexural makers into layer thicknesses and depth below seabed, and to best estimate bulk layer density. In turn, these depths, thicknesses and densities will be used to calculate the 'background' upper plate (crustal) characteristics and load input for 'whole plate' modelling, the results of which will be presented in a subsequent paper.

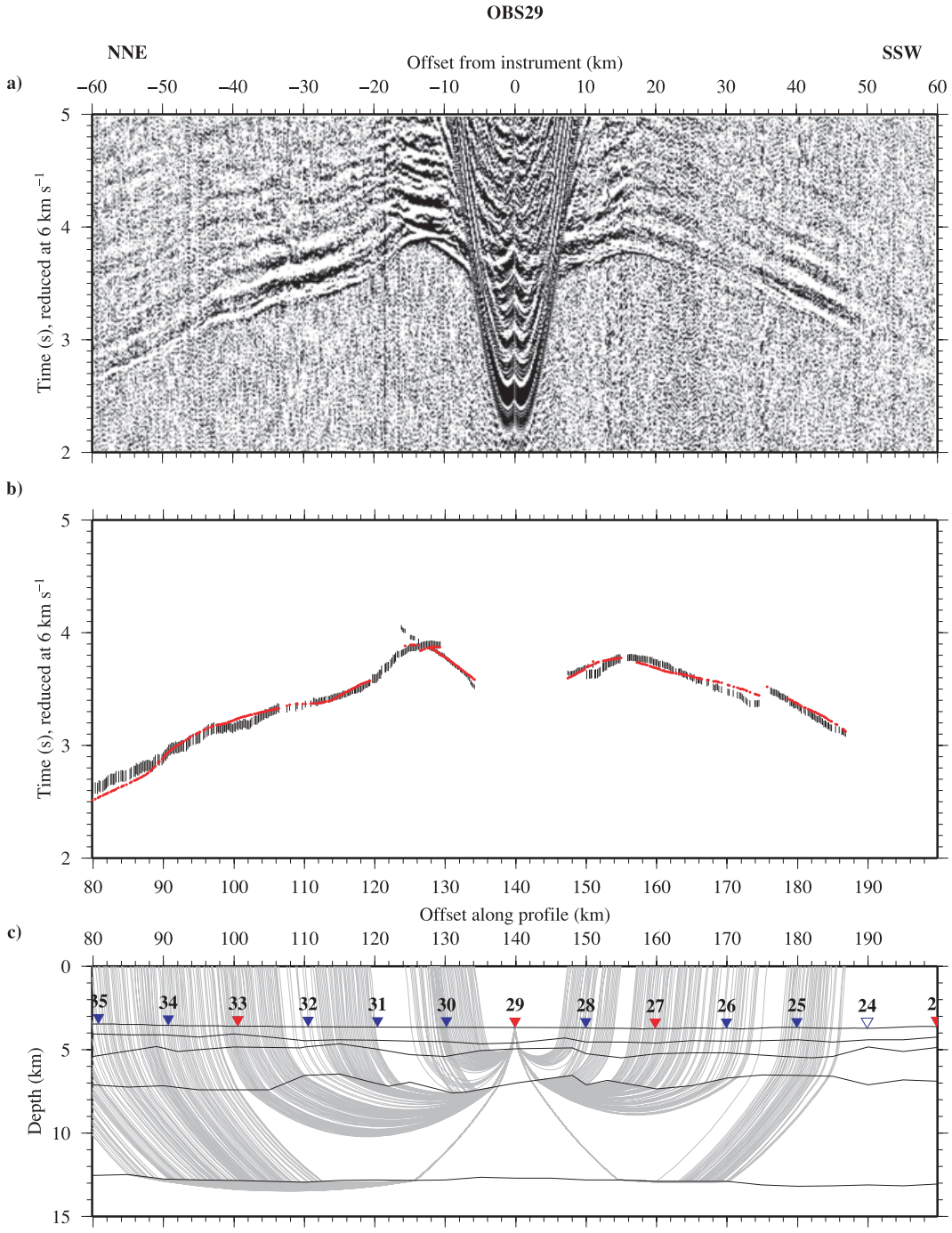


**Figure 6.** Ray-trace modelling of hydrophone data recorded by OBS 29. See Fig. 4 for details.

### 5.5 Traveltime picking

For traces with clear primary arrivals, the onset of the seismic wavelet was picked. Uncertainties, summarized in Table 1, were assigned according to offset as detailed above, and accounting for the decrease in SNR due to spherical divergence, scattering and absorption of the seismic energy. However, for secondary arrivals, and primary arrivals with low SNR, the zero-crossing immediately before the arrival waveform's first peak was picked and the assigned uncertainties adjusted accordingly.

## 6 SEISMIC MODELLING

A 2-D *P*-wave velocity–depth model of the crustal structure at the Cape Verde Swell has been created by combining the analysis of coincident MCS data, to constrain the shallow subsurface, with forward modelling of the WA data to obtain the structure of the oceanic basement and uppermost mantle. Sensitivity testing of velocity and depth nodes has also been conducted to determine the limits of model resolution. Finally, standard velocity–density relationships have been used to calculate the FAA to compare with that observed,

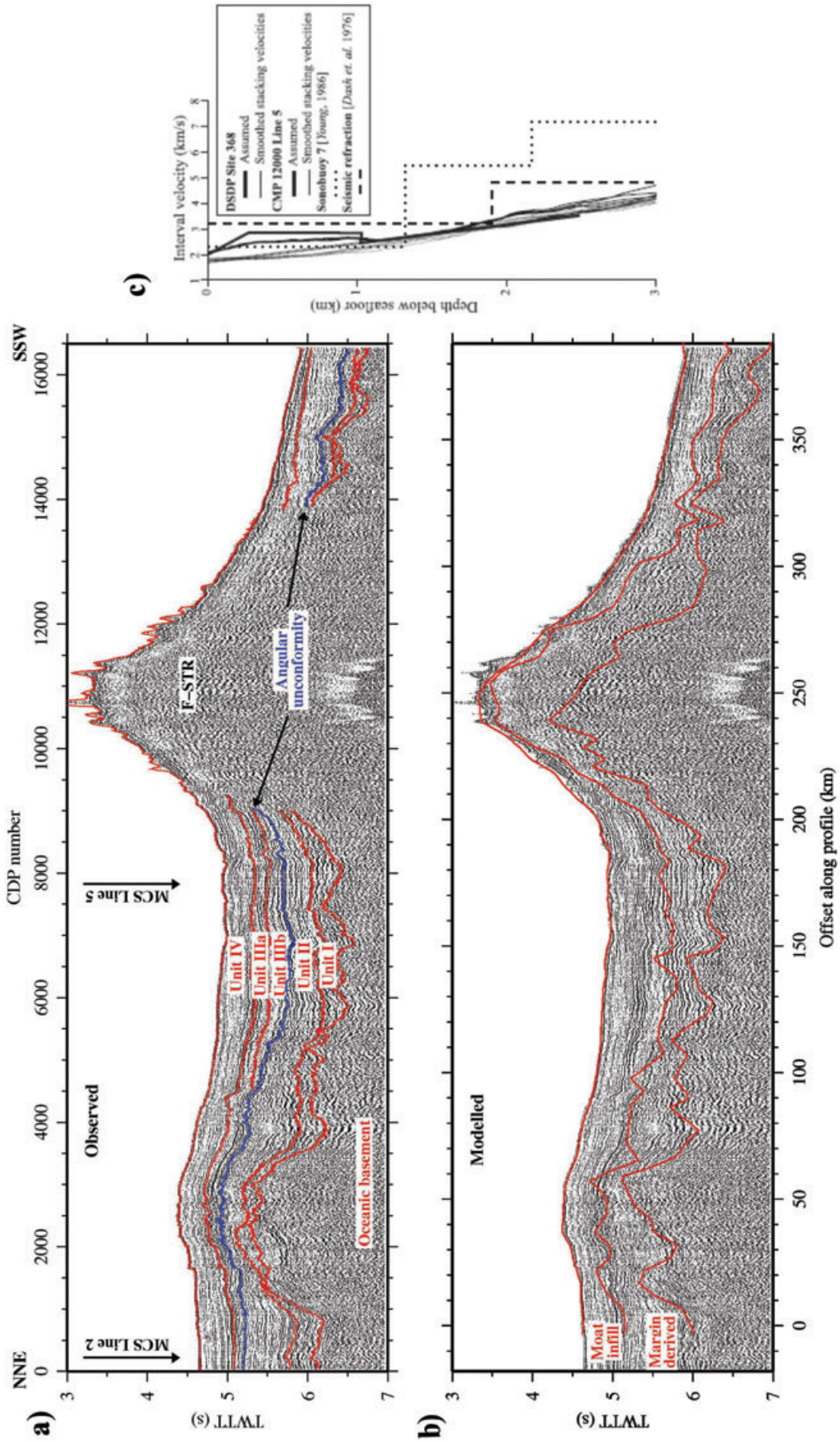


**Figure 7.** Comparison of the shallow subsurface layers picked from the MCS data with the time-converted boundaries from the final best-fitting velocity–depth model. (a) MCS Line 3, coincident with the WA profile of this study, annotated to show the five horizons identified in the sediment column following the seismic stratigraphy defined by Ali *et al.* (2003). The angular unconformity, shown in blue, represents subsidence due to loading and flexure, and defines a change in the primary sediment provenance from the African margin to the Cape Verde islands. Sediment units are named according to the terminology of Ali *et al.* (2003) and tie points with other *RRS Charles Darwin* 1985 MCS lines are indicated with annotated arrows. (b) Time-converted boundaries from the final 2-D velocity–depth model. The model boundaries, although more undulating, correspond with the originally interpreted positions of the angular unconformity and the top-basement reflector and agree well with distinct changes in reflector characteristics, giving confidence in the shallow model structure. (c) Summary of 1-D velocity–depth profiles (after Ali *et al.* 2003).

**Table 1.** Pick uncertainties and misfits between calculated and observed traveltimes for each phase identified in the WA data set.

| Phase | Pick uncertainty (ms) | Number of picks | rms traveltime (s) | $\chi^2$ value |
|---|---|---|---|---|
| $P_s$ | 20–30 | 712 | 0.036 | 2.654 |
| $P_{g1}$ | 20–30 | 1566 | 0.033 | 2.052 |
| $P_{g2}$ | 30–40 | 8651 | 0.061 | 2.675 |
| $P_mP$ | 50 | 1391 | 0.105 | 4.376 |
| $P_n$ | 40–50 | 4171 | 0.119 | 5.850 |

as an independent check on the viability and uniqueness of the final model, prior to interpretation. Each of these stages will be discussed below, together with a description of the final best-fitting velocity–depth model.

### 6.1 Forward modelling

The best-fitting velocity–depth model was obtained using a 2-D forward ray tracing approach, *rayinvr* (Zelt & Smith 1992), and assuming that, in this locality, 3-D crustal heterogeneity has little affect on ray propagation, i.e. the crustal structure of the swell is effectively axisymmetric except immediately in the vicinity of each island of the archipelago. The initial starting model was populated with two types of nodes for each layer; depth nodes describe the upper boundary geometry, while velocity nodes define vertical and horizontal velocity gradients.

In the initial model, the water column was included as a single layer whose base, the seabed, was defined using the shipboard swath bathymetry data. This layer was assigned a velocity of 1.49 km s$^{-1}$ at the top (sea level) increasing to ∼1.51 km s$^{-1}$ at the seabed. Immediately beneath the water column, the two sediment layers are defined using *P*-wave velocity estimates taken from DSDP site 368 core analysis (Lancelot *et al.* 1978), together with stacking velocities used to process the MCS record sections (Fig. 7c; Ali *et al.* 2003), to depth convert the intrasediment unconformity and basement surface picked from the MCS section (Fig. 7a). Finally, a simplistic, one-dimensional, two-layered oceanic crustal basement, with underlying lithospheric mantle, was incorporated to complete the initial model using layer thicknesses, velocities and velocity gradients derived from White *et al*.'s (1992) model for standard, mature Atlantic oceanic crust.

Prior to subseabed modelling, instrument locations and the seabed topographic profile were checked using the direct water wave arrival and the seabed-sea surface multiple. Following ray tracing, minor adjustments to instrument locations and seabed depth were made, where needed, to obtain a fit within the picking errors for the two sets of water column arrivals.

A top-down approach was adopted for modelling, tracing progressively deeper layers to calculate arrivals to increasing shot-receiver offsets. For each layer, the arrivals from a subset of four-to-five adjacent instruments were modelled simultaneously, starting at the northern end of the profile. A 'rolling window' technique was adopted to progressively incorporate additional instruments along the profile while maintaining an overlap with the previous subset.

The fit of calculated arrivals to the traveltime picks was initially qualitatively assessed to produce a model that approximately satisfied the observed data. Subsequently, analysis of rms traveltime misfit and the $\chi^2$ parameter (Zelt & Smith 1992) provided a quantitative assessment and acted as a statistical indicator when making minor adjustments to further refine the fit of the model.

The results of modelling are demonstrated by a selection of record sections and matching ray diagrams shown in Figs 4–6, and a summary of the assigned uncertainties, number of picks, rms misfit and $\chi^2$ values for each of the identified phases can be found in Table 1. For reference, a $\chi^2$ of 1 is considered a good fit, while a $\chi^2$ of $<1$ is an over-fit to the observed traveltime picks. In this study, a $\chi^2$ of $<5$ is considered an acceptable fit.

## 7 RESULTS

The best-fitting velocity–depth model (Fig. 8a) is 475 km long, with instruments located between 30 and 420 km model offset. Shots were fired from north to south between 0 and 474 km profile offset. The best-fitting model can be summarized as a succession of two discrete sedimentary packages overlying typical two-layered oceanic basement, which shows only slight thickening between the adjacent islands of the archipelago at the F-STR. A brief description of each model layer is included below.

### 7.1 Sediment layers

The first, shallowest, layer subseabed is interpreted as a sequence of moat infill sediments and it is present along the entire profile. Although relatively thin at the northern limit of the model, the infill reaches a maximum thickness of 1 km at ∼150 km profile offset, with velocities of 2.0–2.5 km s$^{-1}$. These infill sediments almost pinch out over the F-STR before returning to an average thickness of 0.7 km at profile offsets >320 km, where slightly higher velocities of 2.5–2.7 km s$^{-1}$ are also observed. This range of *P*-wave velocities matches those recorded by Lancelot *et al.* (1978) for the marls and claystone turbidites observed up to 1 km below the seabed at DSDP site 368.

Although originally included in the model to reflect a package of terrigenous sediments derived from the African margin, the second, deeper, layer subseabed exhibits the most lateral variation in *P*-wave velocity within the entire best-fitting final model. In the final model, this layer generally exhibits an average thickness of $<1$ km and *P*-wave velocity of 3.0 km s$^{-1}$. However, between 210 and 310 km profile offset, this layer thickens to a maximum of 2.2 km with velocities of 3.5–4.5 km s$^{-1}$, constrained by the $P_s$ phase observed on the mid-profile OBSs. This higher velocity region, concurrent with the bathymetric high of the F-STR, suggests the possibility that the emplacement of extrusive volcanic material to the crust at the Cape Verde Swell may not be localized entirely to the islands. Alternatively, analysis of the Hydrosweep swath bathymetry collected in this area shows a highly irregular, hummocky region with partly buried volcanic cones suggesting that at least part of the F-STR may comprise volcaniclastic debris from past landslide and flank collapse events originating on the adjacent islands of Fogo and Santiago (Day *et al.* 1999; Masson *et al.* 2008).

Due to the limited number of observed arrivals from the sedimentary layers, much of the shallow structure has been modelled using the deeper propagating ray groups. However, this approach does not always provide a unique solution due to the complex interrelationship between boundary geometries and velocities when modelling several nodes at once. As a means of continuously checking the geometry and velocity of the sedimentary layers as modelling progressed, the depth of the unconformity and top-basement horizons were converted back into two-way traveltime (TWTT) using the model-derived velocities and compared with the MCS data as an independent check for consistency (Fig. 7b).

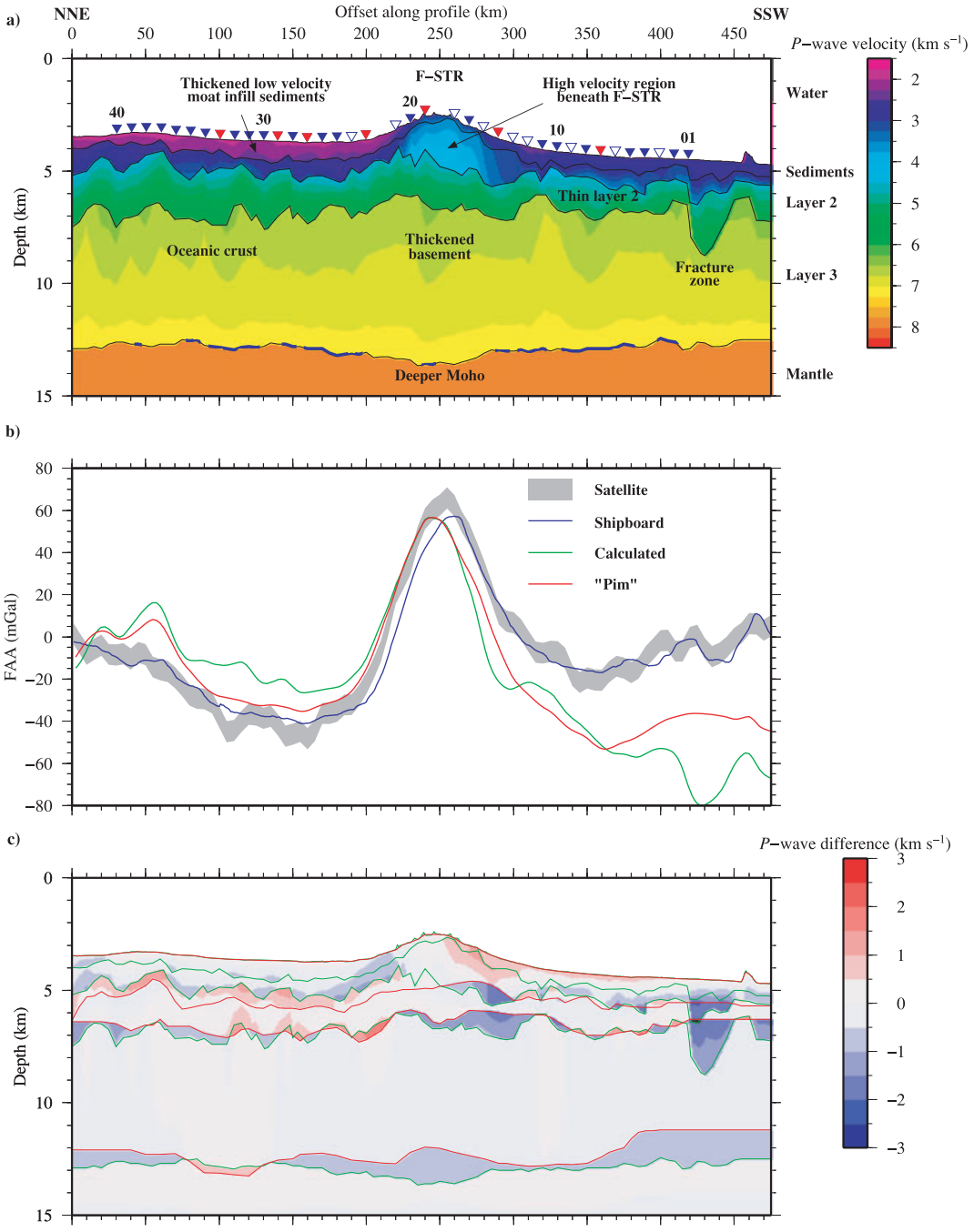


**Figure 8.** Best-fitting velocity–density–depth model. (a) Final velocity–depth model. The layer boundaries taken from the *rayinvr* model file are shown as solid black lines. Blue shading on the Moho indicates regions constrained by $P_mP$ arrivals. Note that the mid-lower crust is only well constrained by crossing ray paths between *ca*. 40 and 425 km model offset, which may contribute to the misfit between the observed and calculated free-air gravity anomaly outside this region. See Figs 10–12. Key features, as discussed in the text, are labelled. OBS locations are shown by the inverted triangles. See Fig. 2 for transect location, definitions and abbreviations. (b) Comparison of the free-air gravity anomaly observed along the profile with the anomalies calculated from the best-fitting seismic model in (a) (see Fig. 12 for density information) and the model of Pim *et al*. (2008). (c) Difference between the best-fitting model and that of Pim *et al*. (2008) (Fig. 9). See text for discussion. The 'Pim' model layers are shown by solid red lines, this study by green.

In the final model, the mid-sediment model boundary correlates well with the angular unconformity in the MCS data; this can be seen most clearly between 75 and 190 km profile offset and it separates an acoustically transparent layer containing occasional chaotic reflectors, from a highly stratified package of moderate amplitude reflectors. The top-basement surface follows the lowest coherent, high-amplitude reflector. Beneath this surface the characteristic hummocky reflector pattern of the upper surface of the oceanic basement is evident.

### 7.2 Crustal layers

The oceanic basement was modelled as two layers to match the distinct crustal phases observed in the data. A second-order

discontinuity within the crust was required to accommodate a decrease in vertical velocity gradient, interpreted to represent the transition from the pillow basalt and dykes of layer 2 to the gabbros of layer 3 (White *et al.* 1992).

The top-basement surface is coarsely hummocky, with irregular undulations of amplitude 0.5 km and wavelength >15 km, and at an average depth below sea level of 5.25 km. There are two prominent basement highs >1 km shallower than the average depth of the top-basement surface: the first is located at 20–50 km profile offset, where a peninsula of shallower bathymetry extends west from Sal (Fig. 2); the second is located beneath the northern edge of the F-STR. A basement low, 1 km below the average depth of the top-basement surface is located at 420 km.

There is little lateral variation in the velocity structure of the crust along the profile, with average values for the upper and lower layers of 5.4 and 6.9 km $s^{-1}$, respectively. The total crustal thickness increases from the north towards the F-STR as a consequence of the basement high and the slightly increased depth of the Moho, reaching a maximum thickness of 9 km at 230 km profile offset. Despite the observed thickening of the basement, there is no evidence of high *P*-wave velocities (>7.3 km $s^{-1}$) associated with crustal underplate (e.g. Charvis *et al.* 1999).

The maximum depth of penetration of rays traced through the lower crust is ∼11 km below sea level, which is on average 2 km shallower than the modelled Moho. The velocity structure of the deepest parts of the crust is, therefore, constrained by modelling the $P_n$ and $P_mP$ ray groups, the result of which is described in the next section.

To the south of the F-STR, between 320 and 420 km profile offset, the crust thins to 7 km, with most of the thinning accommodated in the upper crust. Beneath OBS 01, at the southern end of the profile, a large subvertical fault is interpreted to traverse the entire upper crust. This fault is located at the southern end of the region of thin upper crust and gives rise to the basement low described above. This upper crustal structure resembles a cross-section through an oceanic transform fault (e.g. White *et al.* 1984), indicating the possible location of an Atlantic fracture zone.

Many fracture zones have been interpreted to cross the Cape Verde region in an E-W orientation, perpendicular to the WA profile, through the correlation of offsets in magnetic anomaly lineations (e.g. Williams *et al.* 1990). The topographic relief of fracture zones is often concealed by pelagic sedimentation. However, the gravity anomaly due to the vertical offset of the top-basement surface is sometimes observed on profiles perpendicular to the fault.

The first derivative (in latitude) of the Sandwell & Smith (1997) 1 × 1 min global gravity dataset is a useful way to highlight the relatively short-wavelength ridges and troughs associated with fracture zones in the region of long-wavelength mid-plate bathymetry swells (Fig. 2c). Several lineations can be seen trending from west to east across the Cape Verde Swell, which correlate with known fracture zones (including Kane and Fifteen-Twenty) interpreted from the bathymetry of the Mid-Atlantic Ridge axis. One of these observed lineations intersects the WA profile at its southern end where the anomalous crustal structure has been incorporated into the model, providing supporting evidence for its interpretation as a previously unmapped fracture zone in the region.

### 7.3 Moho and upper mantle

The topography of the Moho is very subdued, with an average Moho depth of 13 km below sea level, which increases slightly to 13.5 km beneath the F-STR, at 250 km profile offset. The primary constraint on the depth to the Moho comes from arrivals reflected at the crust-mantle interface, the $P_mP$ phase. Unfortunately, the $P_mP$ phase is not clear on all records, and is particularly difficult to identify in the centre of the profile where records have a lower SNR, and clear arrivals are only observed at near offsets. Also, without further control on the velocity structure of the lower crust (>10 km depth), the error in the position of the Moho remains relatively large due to the trade-off between the interval velocity and thickness of the lower crustal layer.

On records with clear arrivals at shot-receiver offsets >30–40 km, the $P_n$ phase can be identified and this provides a control on lower crustal velocities, allowing Moho depth to be independently modelled. The upper mantle velocity directly below the Moho is 7.9 km $s^{-1}$ and a slight positive gradient in the mantle is required in order to turn the $P_n$ rays, with 8.0 km $s^{-1}$ assigned to the base of the model at 40 km depth. The absence of arrivals at >70 km shot-receiver offset throughout the dataset means that only the velocity of the upper mantle directly beneath the Moho is known directly.

### 7.4 Resolution

The goodness of fit of the final model was assessed using the rms traveltime and the $\chi^2$ parameter. However, these parameters only reflect the statistical fit between the calculated arrivals and the observed picks. In order to test the resolution of the model, a sensitivity test was conducted in which seismic velocities and boundary depths were systematically varied and the fit reassessed. In resolution terms, a model was considered an acceptable fit as long as the difference in calculated and observed traveltimes did not exceed twice the standard error assigned to the picks. This analysis shows that *P*-wave velocities may differ by ±0.2 km $s^{-1}$ in the sediment layers and by up to ±0.5 km $s^{-1}$ in layer 3 and an acceptable fit is still achieved. On the same basis, the depth to the top of the oceanic basement is estimated to lie within ±0.2 km of the best-fitting model interface at worst, and the depth to the Moho is estimated to lie within ±1.5 km.

### 7.5 Comparison with Pim *et al*. (2008)

It is at this point worth directly comparing our best-fitting model (Fig. 8) with that from the pilot study of Pim *et al*. (2008) (Fig. 9—henceforth the 'Pim' model) using the data from just nine of the OBSs. Fig. 8(c) shows a difference plot between the two models where the 'Pim' model has been subtracted from our model. In general, the models are very similar which in one sense is reassuring, but in another sense is somewhat surprising given the significantly fewer and more widely spaced OBSs used to derive the 'Pim' model. The main differences between the two models are as follows.

1. The trade-off between the two sediment column and oceanic layer 2 thicknesses, with the velocity–depth profiles within each layer being effectively equivalent.
2. The rougher sediment–layer 2 and layer 2–layer 3 interfaces in our model, especially so at the SSW end of the model where a significant intrabasement offset discontinuity is implied, which could reflect a fracture zone.
3. The incorporation of all 38 OBS datasets leads to, on average, a 1–2 km deeper but less vertically varying Moho, although the velocity–depth profile in ocean layer 3 in both models is effectively equivalent.

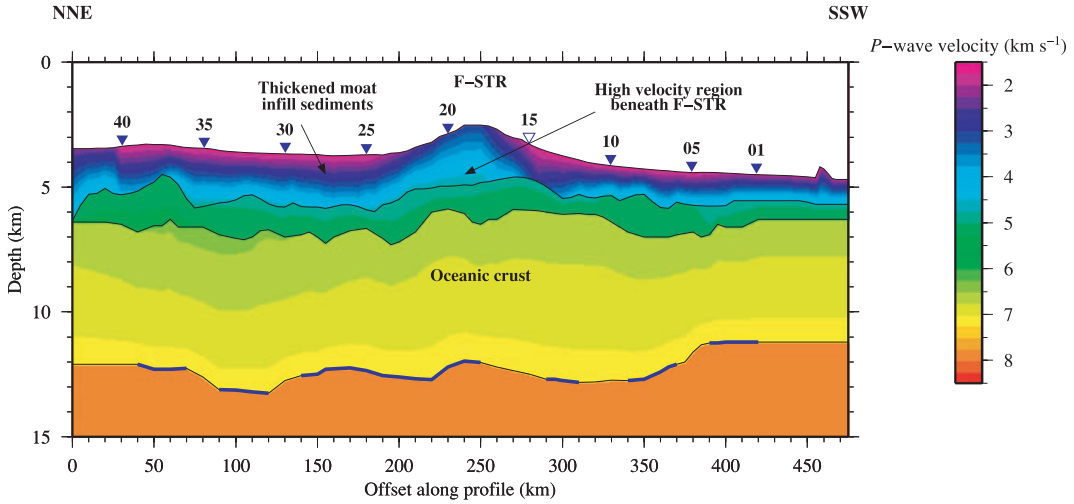


**Figure 9.** Best-fitting velocity–depth model of Pim *et al*. (2008). The layer boundaries taken from the *rayinvr* model file are shown as solid black lines. Blue shading on the Moho at *ca*. 12 km below sea level shows the constraint provided by $P_mP$ arrivals. Key features, as discussed in the text, are labelled. The locations of the nine OBS used to develop this model are shown by the inverted triangles. See Fig. 2 for transect location, definitions and abbreviations.

4. The velocity–depth structure on the margins of the F-STR is aliased in the 'Pim' model towards the locations of the two OBS that constrain its shallow. structure.

Although the simpler and smoother 'Pim' model is likely to be more geologically realistic considering the resolution versus depth capabilities of the various methods used to acquire and analyse the data, the denser subsurface sampling achieved by the entire dataset results in, statistically, a better fit, especially when considering layer interface geometries and velocity transitions across interfaces. Also, given the limited depth of signal penetration subsurface, the depth and geometry of the Moho in our model is likely to be a more accurate representation not only of the lower crust and uppermost mantle velocity structure (and hence more definitive in terms of likely existence of lower crustal underplate/intrusion) but also Moho geometry.

A further, and probably obvious, conclusion that can be drawn is that in regions of rapid change in seabed bathymetry or likely significant lateral change in velocity and layer thickness, it is better to deploy more closely spaced instruments over and either side of such features, while for more subdued or strike-line type profiles, more widely spaced instruments may provide more than adequate subsurface imaging and resolution at all crustal depths.

## 8 GRAVITY MODELLING

The uniqueness of the best-fitting velocity–depth model was also tested by calculating the gravity anomaly for the corresponding density–depth model and comparing this to both the Sandwell & Smith (1997) 1×1 minute global free-air gravity dataset and the higher-resolution shipboard data (Fig. 8b) acquired during seismic acquisition. In addition, gravity modelling also offers the potential of additional constraint on the deeper parts of the model otherwise not well constrained by seismic arrivals.

For all gravity modelling presented in this paper, a 2-D approach was adopted in which a block density model was derived from the *rayinvr* best-fitting velocity–depth model and standard velocity–density relationships for sediments and oceanic crustal rocks were used to convert velocities to densities (Hamilton 1978; Carlson & Raskin 1984; Carlson & Herrick 1990). Model layer boundaries and iso-velocity contours were used to divide the model into a succession of layers and blocks which were assigned interval density values in the range 1750–2950 kg $m^{-3}$, with fixed water column and mantle densities of 1030 and 3330 kg $m^{-3}$, respectively. The 2-D gravity program, *grav2d*, written by J.H. Leutgart and based on the algorithm of Talwani *et al*. (1959), was then first used to calculate the gravity anomaly for the modelled crustal structure beneath the profile (Figs 8a and b), and then for assessing the likely origin of the observed long-wavelength component in the FAA discussed later.

Based on the seismic model alone, the calculated FAA shows a reasonable agreement with the short and medium wavelength features in the observed data; the small highs at 60 and 400 km profile offset, and the main peak at 250 km profile offset, respectively. However, the calculated anomaly also contains a long wavelength, effectively linear trend of −0.1 mGal $km^{-1}$ from north to south.

Interestingly, the long wavelength trend implies a density anomaly deeper in the lithosphere, possibly subcrustal. This long-wavelength anomaly may be a result of crustal thickness variations unconstrained by the seismic modelling (i.e. within seismic resolution at Moho depth), or a result of deeper-seated density variation in the mantle, again largely unconstrained by the seismic data.

In order to assess the likely origin of the long-wavelength mismatch, bathymetry and gravity data along a 2500 km extended profile centred on the WA profile were analysed. A simplified two-layer density model of the water column and seabed was constructed (Fig. 10a) to calculate the gravity anomaly due to changes in bathymetry (Fig. 10b). The bathymetry anomaly was then removed from the satellite-derived FAA to obtain the subseabed anomaly. Various 2-D filters were applied in the space domain to the subseabed anomaly to match the long-wavelength low centred at ∼150 km offset. It was not possible to isolate the long wavelength signal south of 150 km due to the medium-wavelength peak at 250 km offset. As a best approximation, a combination long-wavelength signal was created using a cosine filter of width 400 km at the flanks of the profile and a cosine filter of width 100 km between −200 km and 150 km with the filtered signal mirrored about 150 km to fit the long-wavelength trend between 150 km and 500 km, thus assuming it to be symmetrical (Fig. 10c). The long-wavelength signal was subsequently removed from the subseabed anomaly to

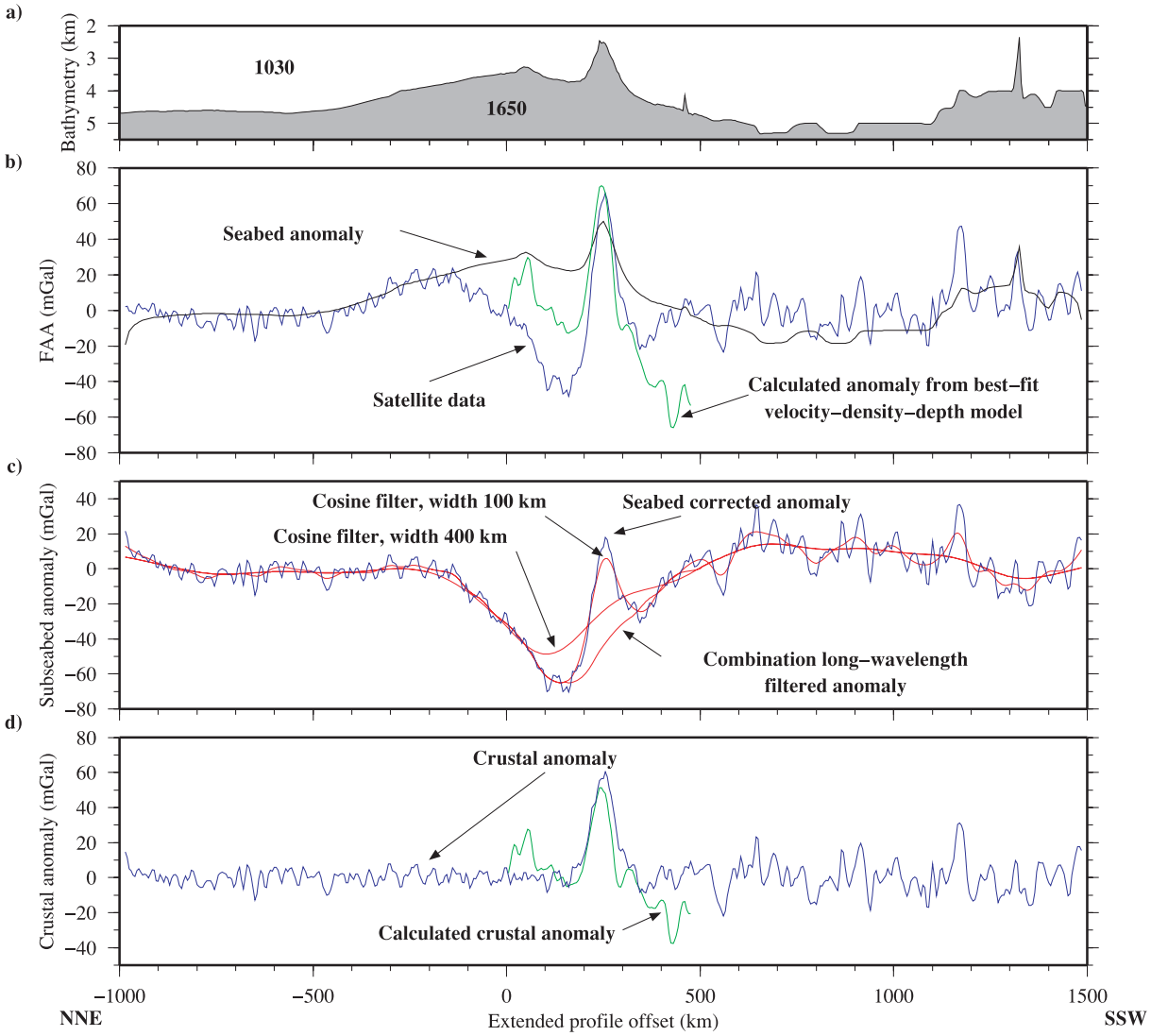


**Figure 10.** Long-wavelength component of the free-air gravity anomaly. (a) and (b) Calculation of the contribution of the seabed alone. Densities are annotated in kg m$^{-3}$. The seabed topography is defined by the combination of GEBCO 1 × 1 min (IOC, IHO & BODC, 2003) and shipboard swath bathymetry data. (c) Deconstruction of the long-wavelength components in the free-air anomaly. (d) Observed crustal component of the free-air anomaly with the long-wavelength component removed (blue line) compared with the anomaly calculated from the best-fitting velocity–density–depth model of Fig. 8 with the seabed anomaly removed (green line).

reveal the 'crustal' anomaly, which has been compared to the output from the best *rayinvr* model with the bathymetry anomaly removed (Fig. 10d). The observed and calculated crustal anomalies show a reasonable agreement between 100 and 350 km offset but diverge at the extremities of the model.

Before testing the sensitivity of the density–depth model to subtle changes in the crustal density structure, the possible origin of the long-wavelength anomaly will be investigated. Firstly, the crustal density model was modified to incorporate lateral variations in the density of the lithospheric mantle by incorporating a region of low density (relative to 'normal' mantle) centred at 150 km offset. A range of density contrasts, compensation depths and low-density region widths were tested in an attempt to reproduce the amplitude of the long-wavelength anomaly. The example model shown in Fig. 11(b) is clearly non-unique. However, with a density contrast of 30 kg m$^{-3}$ and compensation depth of 100 km, the subcrustal gravity anomaly calculated using this model (Fig. 11a) matches the amplitude of the long-wavelength signal. However, its wavelength characteristics are not well matched, suggesting that the low-density region may have gradual lateral density transitions rather than the sharp boundaries modelled here.

The density–depth model of Pim *et al.* (2008) also has a low-density region in the lithospheric mantle, between ∼50 and ∼250 km offset. However, several other short-wavelength mantle density variations are also incorporated into the Pim *et al.* (2008) model which may produce the necessary gradational transition outlined above. The major difference to the model presented here is the magnitude of the density contrasts (maximum 160 kg m$^{-3}$), which is a direct result of the shallow compensation depth (16 km) that Pim *et al.* (2008) use. However, the model presented here is considered a better solution because its deeper compensation depth better matches estimates from other studies of the swell (e.g. McNutt 1988) and the more regional-scale low density anomaly in the lithospheric mantle beneath the Cape Verde islands which, in turn, better fits the passive seismological models of Lodge & Helffrich (2006).

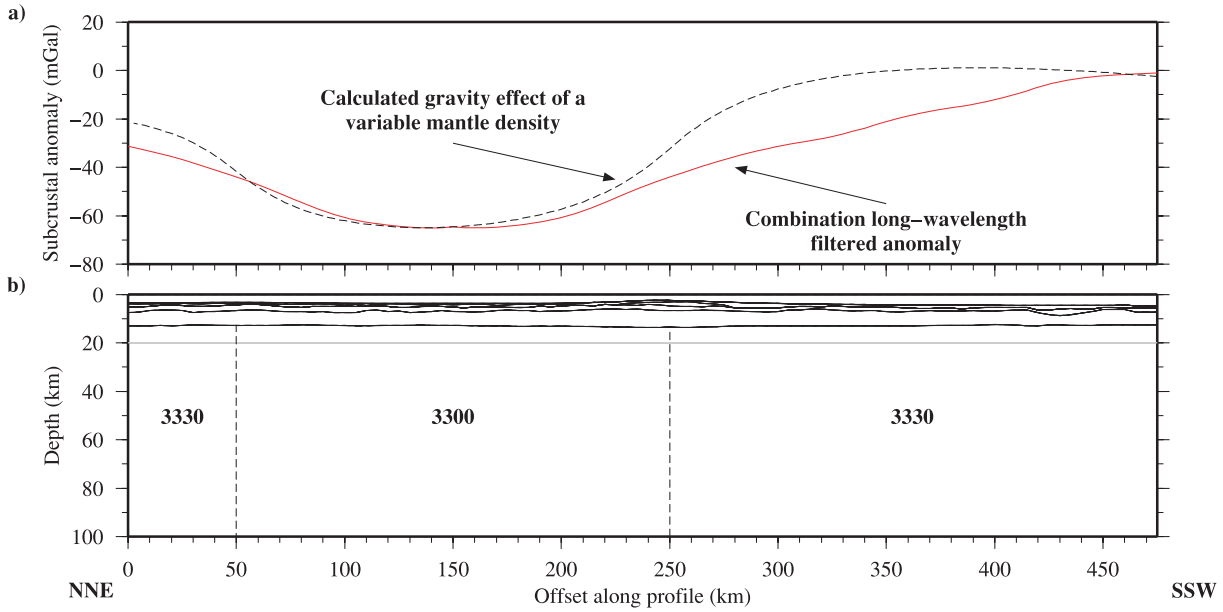


**Figure 11.** Modelling of the long-wavelength component free-air gravity anomaly. a) and b) Modelling of the long-wavelength anomaly (red line) shown in Fig. 10, by a laterally varying mantle and a compensation depth of 100 km (black dashed line). Densities are annotated in kg $m^{-3}$.

The fit of the crustal gravity anomaly will now be considered. Variations in the total crustal thickness were modelled in an attempt to account for the misfit at the extremities of the model (<50 km model offset; >350 km offset). A 1 km increase in the depth of the Moho between 0 and 60 km and a gradual decrease of up to 2 km from 325 to 475 km improved the fit of the flanking regions of the crustal anomaly to the observed data (Figs 12a–c). The adjustments made to the depth of the Moho only exceed the uncertainties of the seismic model at the southern end of the model, past the maximum extent of the WA seismic data coverage.

As the best-fitting seismic model provides limited constraint on the lower crust, a further series of tests were conducted to investigate whether the gravity modelling is sensitive to the presence of underplate, and if so, to what resolution limits. To undertake these tests a series of modifications were made to the best-fitting seismic model to represent the presence of various thicknesses of underplate beneath the crust and magmatic intrusion into the lower crust. These modifications were constrained to range from below to above the seismic resolution in velocity (hence density) and interface geometry at Moho depth.

A range of velocity–depth models were created in which a layer of underplate with *P*-wave velocities ranging from 7.3 to 7.8 km $s^{-1}$ (e.g. Morgan *et al.* 1989) was incorporated below the Moho or within the lower crust using a cosine function centred at 250 km profile offset with a width of 150 km and amplitudes ranging between ±5 km to perturb the Moho in the best-fitting model. Following each modification, the fit to the seismic data was reassessed and the FAA recalculated to show the change in the crustal gravity anomaly, which is manifest mainly in the amplitude of the peak. Modelling shows that, within the seismic data resolution in the lower crust and at the Moho, it is possible that up to a 3 km thickness of 'underplate' (i.e. within the lower crust and/or within the mantle) could be incorporated into the model to improve the fit to the peak FAA without significantly reducing the fit to the seismic data (Figs 12d and e). Combining the changes in crustal thickness and the maximum extent of any potential intracrustal magmatic intrusion produces a final model (Fig. 12f) that fits the main features of the observed crustal anomaly, suggesting that a small amount (up to 3 km maximum thickness) of magmatic material (either as underplate or intrusion) may be present at the base of the oceanic crust, located beneath the F-STR. A similar feature is observed at the Louisville Seamount chain in the SW Pacific (Contreras-Reyes *et al*. 2010).

The main conclusions that can be drawn from the gravity modelling are as follows.

1. Investigation of an extended profile through the Cape Verde Swell indicates that a long-wavelength FAA low exists at the northern half of the WA profile, and subsequent 2-D modelling suggests that the origin of this anomaly is within the lithospheric mantle.
2. A model incorporating lateral variations in mantle density can account for the long-wavelength low and is similar to that described by Pim *et al.* (2008), although here we demonstrate a compensation depth which is in accord with other studies (McNutt 1988; Lodge & Helffrich 2006). The area of low density mantle agrees well with the boundaries of the archipelago and a decrease in the observed heat flow anomaly (Fig. 2)
3. The seismic model is fairly unique in that it provides a good basic fit to the short and medium wavelength features in the crustal component of the FAA.
4. Up to 3 km of material of higher density than the crust could be incorporated at its base beneath the F-STR, within the errors of both the seismic and the gravity modelling.

## 9 DISCUSSION

The Cape Verde archipelago is situated on the crest of the largest observed hotspot swell on Earth, making it the ideal location to conduct a detailed geophysical investigation of proposed swell and plate load support models. The results of 2-D seismic and gravity modelling presented in this paper, are the first steps to testing the various models proposed and, in turn, may provide a better understanding of the origin and evolution of the Cape Verde Swell. The models that have been proposed to explain how the large-scale

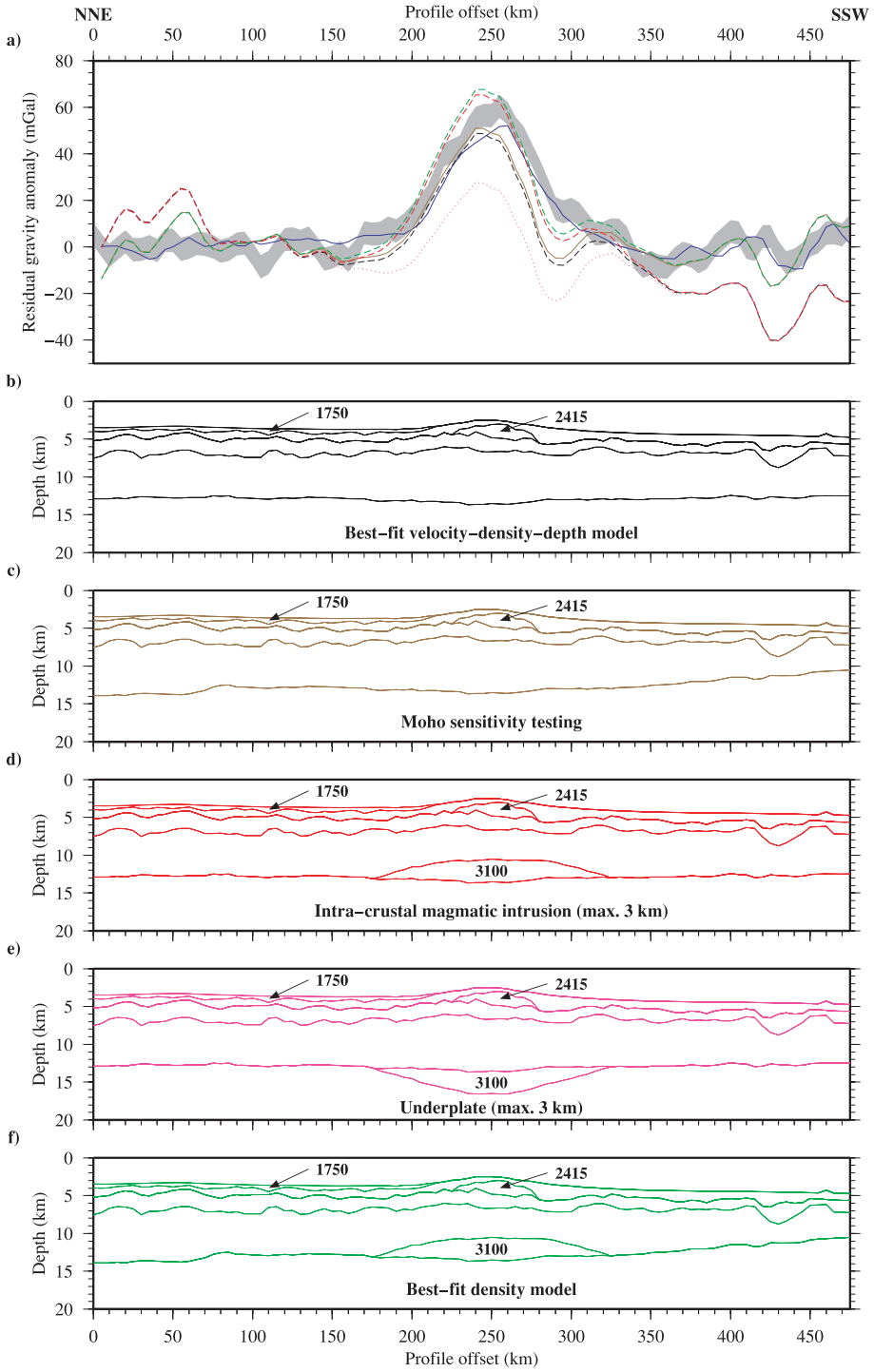


**Figure 12.** Sensitivity testing of the crustal density–depth model. (a) Comparison of the free-air gravity anomaly observed using satellite measurements (grey band including error) and shipboard data (blue line) with the gravity anomaly calculated from the final density–depth models shown in (b)–(f). Note that the long-wavelength component of the observed free-air anomaly (Fig. 10) has been removed. The density constants used for the water column (1030 kg $m^{-3}$), shallow subsurface layer (2010 kg $m^{-3}$), oceanic layer 2 (2630 kg $m^{-3}$) and layer 3 (2930 kg $m^{-3}$), and the mantle (3330 kg $m^{-3}$) are consistent for all models shown in (b)–(f), other densities specific to isolated regions are annotated in kg $m^{-3}$. For parts (b)–(f) of this figure, the colour coding of the model corresponds to the colour coding of the associated calculated anomaly plotted in (a). See text for discussion.

topographic swells associated with hotspots are sustained over geological timescales can be briefly summarized as:

1 – shallow support within the crust (e.g. Morgan *et al.* 1995),
2 – support within the upper mantle (e.g. Detrick & Crough 1978; Robinson, 1988), and
3 – dynamic mantle upwelling (e.g. Sleep, 1995).

Shallow crustal support would be evidenced by a thicker than average oceanic basement, originating either at the time of formation at a mid-ocean ridge due to above average magmatic accretion or during island building by the synchronous addition of magmatic

underplating to the base of the crust. Assuming a simplified block model of the lithosphere under Airy isostatic equilibrium, the igneous layer within the oceanic crust would have to be ∼15 km thick in order to support the ∼2 km high swell observed at the Cape Verdes, placing the Moho at ∼17.5 km depth below sea level, 4 km deeper than is observed and well outside the best-fitting modelled Moho error bounds as demonstrated by the sensitivity testing.

Instead, the final velocity–depth model shows an igneous section that is 8 km thick on average, well within the range expected for standard oceanic crust (White *et al.* 1992), and similar to that observed in the pilot study conducted by Pim *et al.* (2008), although the crust does appear to slightly thicken towards the centre of the profile beneath the F-STR, to a maximum of 9.5 km. High shallow crustal velocities suggest, however, that the thickening is accommodated within the upper crust either by extrusion as part of island emplacement or as a high velocity volcaniclastic debris deposit on top of the basement, a consequence of adjacent island failure. Analysis of the detailed swath bathymetry data in the area better supports the latter possibility, with evidence of mass transport from the adjacent island of Fogo (Day *et al.* 1999; Masson *et al.* 2008). Receiver function analysis (Lodge & Helffrich 2006) suggests that crustal thickening, perhaps by magmatic underplating, may be more prolific beneath the islands where Moho depths up to 20 km are inferred. There is no evidence from this study to suggest that such an enhanced crustal thickness exists throughout the swell.

Additionally, there is no direct evidence from the seismic data for lower crustal velocities $>7.3$ km s$^{-1}$, a common feature observed at oceanic islands which show significant volumes of underplated material (e.g. Caress *et al.* 1995). However, it is possible that a thin layer of magmatic underplate exists at or within the base of the oceanic crust, that is below the resolution and constraint provided the WA seismic data, given the degree of uncertainty on the depth of the Moho and on lower crustal *P*-wave velocities.

Modelling of the FAA provides an independent assessment of the likely presence of underplate, and shows that such a layer with a thickness $<3$ km is possible within the resolution of both the gravity and seismic datasets combined. Although the resolution limits of the WA seismic data do not discount the possibility of crustal underplating, it is certainly not as prevalent at the Cape Verdes as has been observed at other hotspots which have smaller swells (Watts *et al.* 1997), implying that crustal underplating is not the primary cause of swell uplift.

Swell support originating from within the upper mantle due to a region of low density would be evidenced by a long wavelength negative FAA which is not accounted for by the crustal density model alone, implying a deeper (subcrustal) origin. McNutt (1988) calculates, using forward filtering and admittance techniques, that the depth of compensation for the topographic anomaly of the Cape Verde Swell is 69 $\pm$10 km. Lateral changes in mantle density of 20–40 kg m$^{-3}$ account for the misfit of the crustal density–depth model to the FAA, and this corresponds to a velocity difference of 0.25 km s$^{-1}$, which is within the errors of the seismic modelling, making this a realistic solution that satisfies both the gravity and seismic data.

If the density variation is due to elevated temperature as opposed to a change in geochemical composition, then a heat flow anomaly will also be detected. Courtney & White (1986) observed such a heat flow anomaly with peak amplitude of $+16$ mW m$^{-2}$ over the Cape Verde Swell using a series of thermal probe measurements. They show that the magnitude of this anomaly is smaller than expected if the swell uplift is solely the result of the thermal rejuvenation of the lithosphere. In addition, the lateral decrease in upper mantle density required in this study to match FAA modelling is also not sufficient to create the buoyancy required to support the swell topography alone. These findings imply that dynamic mantle upwelling must play a significant role in supporting the Cape Verde Swell.

## 10 CONCLUSIONS

The main conclusions that can be drawn from this study are as follows.

1. The average thickness and velocity structure of the igneous crust beneath the Cape Verde Swell is consistent with that of the standard definition for mature Atlantic oceanic crust of White *et al.* (1992). There is no evidence to support a significantly thickened crust and, consequently, that the swell is supported by a thickened crustal root.
2. At the centre of the WA profile, beneath the F-STR, the only observed crustal thickening along the entire swell transect is attributed to high velocity volcaniclastic material deposited onto the oceanic basement as a result of debris flows from the off-line islands of Fogo and Santiago. Oceanic layer 2 at this location, may also be slightly thickened as a result of magmatic intrusion related to the emplacement of the adjacent islands.
3. Although there is no direct evidence of lower crustal velocities exceeding 7.3 km s$^{-1}$, indicative of magmatic underplating, a thin layer of high velocity material may exist within the resolution limits of the seismic and gravity data ($<3$ km).
4. The long wavelength component of the FAA is not accounted for by the crustal density model alone, suggesting that there is an additional density anomaly deeper within the subcrustal lithosphere. A lateral variation in the upper mantle density of 30 kg m$^{-3}$, above a compensation depth of 100 km, can account for this misfit although it does not alone provide the necessary buoyancy required to support the entirety of the swell topography.
5. The results of this study imply that some form of dynamic upwelling within the asthenospheric mantle must provide the majority of the upward force required to sustain the anomalous topography of the Cape Verde Swell, with minor contributions from both a marginally thickened oceanic crust and partial thermal rejuvenation of the lithospheric mantle.

## ACKNOWLEDGMENTS

DJW was supported by a Durham University Doctoral Fellowship. Seismic data acquisition was funded by the Natural Environment Research Council (grant NER/B/S/2003/00861) and the Deutsche Forschungsgemeinscahft (grants GR1964/5–1 + 7–1). We thank the officers and crew of the R/V Meteor and the sea-going scientists for their efforts. The GMT and Seismic Unix software packages (Wessel & Smith, 1998; Cohen & Stockwell, 2000, respectively) were used to create the figures for this paper. George Hellfrich and an anonymous reviewer are thanked for their positive and helpful comments.

## REFERENCES

Ali, M.Y., Watts, A.B. & Hill, I., 2003. A seismic reflection profile study of lithospheric flexure in the vicinity of the Cape Verde Islands, *J. geophys. Res.,* **108,** 2239, doi:10.1029/2002JB002155.

Caress, D.W., McNutt, M.K., Detrick, R.S. & Mutter, J.C., 1995. Seismic imaging of hotspot-related crustal underplating beneath the Marquesas Islands, *Nature,* **373,** 600–603.

Carlson, R.L. & Herrick, C.N., 1990. Densities and porosities in the oceanic-crust and their variations with depth and age, *J. geophys. Res.,* **95,** 9153–9170.

Carlson, R.L. & Raskin, G.S., 1984. Density of the ocean crust, *Nature,* **311,** 555–558.

Charvis, P. *et al*., 1999. Spatial distribution of hotspot material added to the lithosphere under La Reunion, from wide-angle seismic data, *J. geophys. Res.,* **104,** 2875–2893.

Cohen, J. & Stockwell, J., 2000. CWP/SU: Seismic Unix Release 34: a free package for seismic research and processing, Centre for Wave Phenomenon, Colorado School of Mines.

Contreras-Reyes, E., Grevemeyer, I., Watts, A.B., Planert, L., Flueh, E.R. & Peirce, C., 2010. Crustal intrusion beneath the Louisville hotspot track, *Earth planet. Sci. Lett.,* **289,** 323—333, doi:10.1016/j.epsl.2009.11.020.

Courtney, R.C. & White, R.S., 1986. Anomalous heat-flow and geoid across the Cape Verde Rise—evidence for dynamic support from a thermal plume in the mantle, *Geophys. J. R. astr. Soc.,* **87,** 815–867.

Crough, S.T., 1983. Hotspot swells, *Ann. Rev. Earth planet Sci.,* **11,** 165–193.

Crough, S.T. & Jurdy, D.M., 1980. Subducted lithosphere, hotspots, and the geoid, *Earth planet. Sci. Lett.,* **48,** 15–22.

Cserepes, L., Christensen, U.R. & Ribe, N.M., 2000. Geoid height versus topography for a plume model of the Hawaiian swell, *Earth planet. Sci. Lett.,* **178,** 29–38.

Dash, B.P., Ball, M.M., King, G.A., Butler, L.W. & Rona, P.A., 1976. Geophysical investigation of Cape Verde archipelago, *J. geophys. Res.,* **81,** 5249–5259.

Davis, E.E. & Lister, C.R.B., 1974. Fundamentals of ridge crest topography, *Earth planet. Sci. Lett.,* **21,** 405–413.

Day, S.J., da Silva, S.I.N.H. & Fonseca, J.F.B.D., 1999. A past giant lateral collapse and present-day flank instability of Fogo, Cape Verde Islands, *J. Volc. Geotherm. Res.,* **94,** 191–218.

Detrick, R.S. & Crough, S.T., 1978. Island subsidence, hot spots, and lithospheric thinning, *J. geophys. Res.,* **83,** 1236–1244.

Duncan, R.A. & Richards, M.A., 1991. Hotspots, mantle plumes, flood basalts, and true polar wander, *Rev. Geophys.,* **29,** 31–50.

Grevemeyer, I., Flueh, E.R., Reichert, C., Bialas, J., Klaschen, D. & Kopp, C., 2001a. Crustal architecture and deep structure of the Ninetyeast Ridge hotspot trail from active-source ocean bottom seismology, *Geophys. J. Int.,* **144,** 414–431.

Grevemeyer, I., Weigel, W., Schussler, S. & Avedik, F., 2001b. Crustal and upper mantle seismic structure and lithospheric flexure along the Society Island hotspot chain, *Geophys. J. Int.,* **147,** 123–140.

Grevemeyer, I., Helffrich, G., Faria, B, Booth-Rea, G., Schnabel, M. & Weinrebe, W., 2010. Seismic activity at Cadamosto seamount near Fogo Island, Cape Verdes-formation of a new ocean island? *Geophys. J. Int.,* **180,** 552–558, doi:10.1111/j.1365-246X.2009.04440.x.

Hamilton, E.L., 1978. Sound velocity-density relations in sea-floor sediments and rocks, *J. acoust. Soc. Am.,* **63,** 366–377.

Holm, P.M. *et al*., 2006. Sampling the Cape Verde mantle plume: evolution of melt compositions on Santo Antao, Cape Verde Islands, *J. Petrol.,* **47,** 145–189.

Holm, P.M., Grandvuinet, T., Friis, J., Wilson, J.R., Barker, A.K. & Plesner, S., 2008. An Ar-40-Ar-39 study of the Cape Verde hot spot: temporal evolution in a semistationary plate environment, *J. geophys. Res.,* **113,** B08201, doi:10.1029/2007JB005339.

I.O.C. I.H.O. & B.O.D.C., 2003. Centenary Edition of the GEBCO Digital Atlas, published on CD-ROM on behalf of the Intergovernmental Oceanographic Commission and the International Hydrographic Organisation as part of the General Bathymetric Chart of the Oceans: British Oceanographic Data Centre, Liverpool.

Lancelot, Y. & the Shipboard Scientific Party, 1978. Site 368: Cape Verde Rise, in *Init. Rep. DSDP,* Vol. 41, pp. 233–254, eds Lancelot, Y., Seibold, E. & Gardner, J.V., US Government Printing Office, Washington, DC.

Lodge, A. & Helffrich, G., 2006. Depleted swell root beneath the Cape Verde Islands, *Geology,* **34,** 449–452.

Marty, J.C. & Cazenave, A., 1989. Regional variations in subsidence rate of oceanic plates—a global analysis, *Earth planet. Sci. Lett.,* **94,** 301–315.

Masson, D.G., Le Bas, T.P., Grevemeyer, I. & Weinrebe W., 2008. Flank collapse and large-scale landsliding in the Cape Verde Islands, off West Africa, *Geochem. Geophys. Geosyst.,* **9,** Q07015, doi:10.1029/2008GC001983.

McNutt, M., 1988. Thermal and mechanical-properties of the Cape Verde Rise, *J. geophys. Res.,* **93,** 2784–2794.

McNutt, M.K., Caress, D.W., Reynolds, J., Jordahl, K.A. & Duncan, R.A., 1997. Failure of plume theory to explain midplate volcanism in the southern Austral Islands, *Nature,* **389,** 479–482.

Mitchell, J.G., Lebas, M.J., Zielonka, J. & Furnes, H., 1983. On dating the magmatism of Maio, Cape Verde Islands, *Earth-planet. Sci. Lett.,* **64,** 61–76.

Monnereau, M. & Cazenave, A., 1990. Depth and geoid anomalies over oceanic hotspot swells—a global survey, *J. geophys. Res.,* **95,** 15 429–15 438.

Monnereau, M., Rabinowicz, M. & Arquis, E., 1993. Mechanical erosion and reheating of the lithosphere—a numerical model for hotspot swells, *J. geophys. Res.,* **98,** 809–823.

Morgan, J.P., Morgan, W.J. & Price, E., 1995. Hotspot melting generates both hotspot volcanism and a hotspot swell, *J. geophys. Res.,* **100,** 8045–8062.

Morgan, J.V., Barton, P.J. & White, R.S., 1989. The Hatton Bank continental margin .3. Structure from wide-angle OBS and multichannel seismic refraction profiles, *Geophys. J. Int.,* **98,** 367–384.

Morgan, W.J., 1983. Hotspot tracks and the early rifting of the Atlantic, *Tectonophysics,* **94,** 123–139.

Müller, R.D., Sdrolias, M., Gaina, C. & Roest, W.R., 2008. Age, spreading rates, and spreading asymmetry of the world's ocean crust, *Geochem. Geophys. Geosyst.,* **9,** Q04006, doi:10.1029/2007GC001743.

Parsons, B. & Sclater, J.G., 1977. Analysis of variation of ocean-floor bathymetry and heat-flow with age, *J. geophys. Res.,* **82,** 803–827.

Pim, J., Peirce, C., Watts, A.B., Grevemeyer, I. & Krabbenhoeft, A., 2008. Crustal structure and origin of the Cape Verde Rise, *Earth planet. Sci. Lett.,* **272,** 422–428.

Pollack, H.N., Hurter, S.J. & Johnson, J.R., 1993. Heat-flow from the earths interior—analysis of the global data set, *Rev. Geophys.,* **31,** 267–280.

Pollitz, F.F., 1991. 2-stage model of African absolute motion during the last 30 million years, *Tectonophysics,* **194,** 91–106.

Ribe, N.M. & Christensen, U.R., 1994. 3-dimensional modeling of plume-lithosphere interaction, *J. geophys. Res.,* **99,** 669–682.

Robinson, E.M., 1988. The topographic and gravitational expression of density anomalies due to melt extraction in the uppermost oceanic mantle, *Earth planet. Sci. Lett.,* **90,** 221–228.

Sandwell, D.T. & Smith, W.H.F., 1997. Marine gravity anomaly from Geosat and ERS 1 satellite altimetry, *J. geophys. Res.,* **102,** 10 039–10 054.

Sclater, J.G., Jaupart, C. & Galson, D., 1980. The heat-flow through oceanic and continental-crust and the heat-loss of the earth, *Rev. Geophys.,* **18,** 269–311.

Sleep, N.H., 1992. Hotspot volcanism and mantle plumes, *Ann. Rev. Earth planet Sci.,* **20,** 19–43.

Sleep, N.H., 1995. Geophysics—a wayward plume, *Nature,* **378,** 19–20.

Stein, C.A. & Stein, S., 1992. A model for the global variation in oceanic depth and heat-flow with lithospheric age, *Nature,* **359,** 123–129.

Stillman, C.J., Furnes, H., Lebas, M.J., Robertson, A.H.F. & Zielonka, J., 1982. The geological history of Maio, Cape Verde Islands, *J. Geol. Soc.,* **139,** 347–361.

Talwani, M., Worzel, J.L. & Landisman, M., 1959. Rapid gravity computations for two-dimensional bodies with application to the Mendocino submarine fracture zone, *J. geophys. Res.,* **64,** 49–59.

Turcotte, D.L. & Oxburgh, E.R., 1973. Mid-plate tectonics, *Nature,* **244,** 337–339.

Watts, A.B. & Burov, E.B., 2003. Lithospheric strength and its relationship to the elastic and seismogenic layer thickness, *Earth planet. Sci. Lett.,* **213,** 113–131.

Watts, A.B. & Tenbrink, U.S., 1989. Crustal structure, flexure, and subsidence history of the Hawaiian Islands, *J. geophys. Res.,* **94,** 10 473–10 500.

Watts, A.B. & Zhong, S., 2000. Observations of flexure and the rheology of oceanic lithosphere, *Geophys. J. Int.,* **142,** 855–875.

Watts, A.B., Tenbrink, U.S., Buhl, P. & Brocher, T.M., 1985. A multichannel seismic study of lithospheric flexure across the Hawaiian-Emperor seamount chain, *Nature,* **315,** 105–111.

Watts, A.B., Peirce, C., Collier, J., Dalwood, R., Canales, J.P. & Henstock, T.J., 1997. A seismic study of lithospheric flexure in the vicinity of Tenerife, Canary Islands, *Earth planet. Sci. Lett.,* **146,** 431–447.

Wessel, P. & Smith, W.H.F., 1998. New improved version of the Generic Mapping Tools released, *EOS, Trans. Am. geophys. Un.,* **79,** 579.

White, R.S., Detrick, R.S., Sinha, M.C. & Cormier, M.H., 1984. Anomalous seismic crustal structure of oceanic fracture-zones, *Geophys. J. R. astr. Soc.,* **79,** 779–798.

White, R.S., McKenzie, D. & Onions, R.K., 1992. Oceanic crustal thickness from seismic measurements and rare-earth element inversions, *J. geophys. Res.,* **97,** 19 683–19 715.

Williams, C.A., Hill, I.A., Young, R. & White, R.S., 1990. Fracture-zones across the Cape Verde Rise, NE Atlantic, *J. Geol. Soc.,* **147,** 851–857.

Wilson, J.T., 1963. Evidence from islands on spreading of ocean floors, *Nature,* **197,** 536–538.

Zelt, C.A. & Smith, R.B., 1992. Seismic traveltime inversion for 2-D crustal velocity structure, *Geophys. J. Int.,* **108,** 16–34.